Low-Loss All-Fiber Mode Permuter Design Exploiting Propagation Constant Engineering and Cascaded Long-Period Fiber Gratings

Oleksiy Krutko, *Member, IEEE*, Rebecca Refaee, Anirudh Vijay, *Member, IEEE*, Nika Zahedi, and Joseph M. Kahn, *Life Fellow, IEEE*

***Abstract*—Managing group-delay (GD) spread is vital for reducing the complexity of digital signal processing (DSP) in long-haul systems using multi-mode fibers. GD compensation through mode permutation, which involves periodically exchanging power between modes with lower and higher GDs, can reduce GD spread. GD spread is maximally reduced when the modal GDs of the transmission fiber satisfy a specific relation and the mode permuter exchanges power between specific modes. Mode permuters with fiber Bragg gratings have been developed for links accommodating 6 guided spatial and polarization modes, corresponding to the LP_{01}, LP_{11a}, and LP_{11b} spatial modes in two polarizations; however, to the best of our knowledge, there have been no designs for links supporting a greater number of modes. We present two mode permuter designs based on fiber Bragg gratings for links employing graded-index transmission fibers with 12 guided spatial and polarization modes, corresponding to the LP_{01}, LP_{11a}, LP_{11b}, LP_{02}, LP_{21a}, and LP_{21b} spatial modes in two polarizations. One design utilizes a step-index (SI) transverse profile, and the other features a free-form-optimized transverse profile achieving improved performance. For the SI design, we achieve mode-dependent loss standard deviation (MDL STD) and mode-averaged loss (MAL) of less than 0.14 dB and 0.27 dB, respectively, over the C-band. For the design with a free-form-optimized transverse profile, we achieve MDL STD and MAL of less than 0.11 dB and 0.07 dB, respectively, over the C-band. We numerically evaluate the designs through link simulations and quantify the reduction in GD spread for different levels of random inter-group coupling in the fiber. Our results show that in a link with periodic mode permutation and mode scrambling, the GD STD is reduced by a factor over 3.13 compared to a link relying solely on periodic mode scrambling.**

***Index Terms*—Fiber Bragg gratings, optical fibers, optical fiber communication, optical fiber dispersion.**

I. Introduction

POWER-LIMITED long-haul optical communication systems now utilize space-division multiplexing (SDM) to satisfy the demand for higher data rates. In current SDM systems, cable capacity is optimized under feed-power constraints by employing multiple parallel single-mode fibers (SMFs), with each fiber transmitting a lower power and data rate compared to traditional non-SDM systems [1], [2], [3], [4].

Coupled-core multicore fiber (CC-MCF) and multi-mode fiber (MMF) provide alternatives to SMF, offering the potential to improve integration and scalability in (SDM) systems while increasing capacity per unit fiber [5], [6]. Long-haul links employing MDM in MMF are attractive because they can achieve the highest level of integration [6] and can be efficiently amplified with low mode-dependent gain, while using fewer pump laser diodes per signal mode [7].

High-capacity long-haul MDM links have often used graded-index (GI) MMFs, owing to their relatively low uncoupled GD STD [8], [9]. Within these fibers, the spatial and polarization modes form distinct mode groups. The propagation constants of modes within the same group are nearly identical, whereas those in different groups differ substantially. Random perturbations in these fibers cause strong intra-group mode coupling and weak inter-group mode coupling [10].

Mode-dependent gain and loss (collectively referred to as MDL) and modal dispersion limit the performance of MDM links. Mode scramblers are commonly utilized to introduce strong coupling among all modes to manage these effects [11]. Strong coupling decreases the standard deviation (STD) of link MDL, increasing average capacity and minimizing outage probability [12]. Additionally, it lowers GD STD, reducing the complexity of digital signal processing (DSP) at the receiver. In systems with strong coupling, GD and MDL STDs accumulate in proportion to the square root of the propagation length. Strong mode coupling also improves frequency diversity, which further reduces the outage probability [13].

An alternate method for decreasing GD STD or MDL STD by using mode permutation has also been proposed [14], [15], [16], [17], [18], [19], [20]. Power is periodically exchanged between slow and fast modes or low- and high-gain modes to reduce GD STD or MDL STD accumulation, respectively. Experimental work has demonstrated that mode permutation can achieve GD and MDL STD accumulation in proportion to the square root of the propagation length [15], [16], [17], [21], [22], [23], like standard strong coupling [12], [24], [25], [26]. The authors have

Received 28 August 2025; revised 23 November 2025; accepted 6 January 2026. Date of publication 12 January 2026; date of current version 16 March 2026. This work was supported by Ciena Corporation, Stanford Shoucheng Zhang Graduate Fellowship, and Stanford Graduate Fellowship. *(Oleksiy Krutko and Rebecca Refaee equally contributed to this work.) (Corresponding author: Oleksiy Krutko.)*

The authors are with the E. L. Ginzton Laboratory, Department of Electrical Engineering, Stanford University, Stanford, CA 94305 USA (e-mail: oleksiyk@alumni.stanford.edu; becca24@stanford.edu; avijay@alumni.stanford.edu; nzahedi@stanford.edu; jmk@ee.stanford.edu).

Color versions of one or more figures in this article are available at https://doi.org/10.1109/JLT.2026.3653429.

Digital Object Identifier 10.1109/JLT.2026.3653429

shown that specific mode permutations can result in significantly less GD STD accumulation than an equivalent strongly coupled link [27]. We refer to such a scheme as *self-compensation* due to its similarity in GD accumulation to a link employing conventional GD compensation by concatenation of fibers having opposing modal GD orderings.

We will refer to the physical devices that perform mode permutation as *mode permuters*. Physical mode permuter implementations include photonic lanterns [28], cascaded long-period fiber Bragg gratings (LPFGs) [20], [29], multi-plane light converters (MPLCs) [16], [17], and multiplexer/demultiplexer pairs [21]. Fiber-based options like LPFGs are especially promising as they are integrable, have low device loss and high coupling efficiency over a wide bandwidth, and are readily fabricated via ultraviolet laser exposure, CO_2 laser irradiation, electrical discharge, femtosecond laser exposure, mechanical microbends, or etched corrugations [30], [31], [32], [33], [34], [35], [36], [37], [38].

As with mode scramblers, MDL and MAL requirements are stringent for mode permuters, since signals in long-haul links must traverse tens or even hundreds of these devices. To ensure low GD STD and/or MDL STD across all wavelength channels, mode permuters must also operate over a broad optical bandwidth, such as the C-band. Mode permuters for 6 [39], 12 [21], 20 [23], and 30 spatial and polarization modes [22] have been implemented using multiplexer/demultiplexer (MUX/DEMUX) pairs or multi-plane light converters. However, these devices integrate poorly and incur excessive loss, making them unsuitable for use in long-haul systems. This motivates the need for low-loss, integrated mode permuters. Previous LPFG-based mode permuters have been demonstrated for up to 6 spatial and polarization modes [20], [29], employing cascaded gratings that exchange power between specific mode pairs by leveraging mode field symmetries and phase matching. To the best of our knowledge, an LPFG-based mode permuter for 12 spatial and polarization modes has not yet been demonstrated and is a novel contribution of this work.

Unlike MUX/DEMUX or multi-plane light converter-based solutions, LPFG-based mode permuters are static and non-reconfigurable. Therefore, their mode coupling characteristics must be determined in advance to achieve optimal GD compensation. However, modeling GD accumulation in long-haul links is computationally intensive [12], [24], [25], [26], [27], [28], [40], [41], [42], [43], [44], and therefore effective permutation schemes are typically identified via heuristic or non-exhaustive search methods [16], [17], [18], [19], [20], [21]. Furthermore, the optimality of a permutation scheme is dependent on link-specific parameters such as the transmission fiber's group delay characteristics, [27], [45] so previously reported schemes are not easily transferable across different systems. Accordingly, this paper presents a second key contribution: an analytical method for determining optimal mode permutation schemes for GD self-compensation.

In this work, we provide analytical formulas for evaluating the GD STD of long-haul MDM links employing mode permuters and GI transmission fibers. We use these formulas to study the optimal mode permutations for reducing GD STD in long-haul MDM links employing GI transmission fiber with $D = 12$ spatial and polarization modes. Our analysis shows that GD STD can be minimized by co-design of a transmission fiber and a mode permuter, in which the modal GDs of the transmission fiber must satisfy a certain relation and the mode permuter must exchange power between specific pairs of modes. To create a $D = 12$ mode permuter that meets the required characteristics, we propose a design based on a cascade of LPFGs. Each LPFG is designed to efficiently execute a subset of the necessary mode permutations. To simplify fabrication and minimize splicings, we limit ourselves to inscribing all gratings in the same fiber, which constrains the design of the mode permuter's transverse index profile. We describe the requirements for the propagation constant spacings of the mode permuter fiber to enable high-efficiency mode exchanges with minimal loss and undesired mode coupling. We present two mode permuter designs: one with a step-index (SI) transverse profile, and the other featuring a free-form-optimized transverse profile and yielding better performance. Each design is optimized to minimize loss when splicing into a GI transmission fiber. We examine the efficacy of our designed mode permuters in reducing link GD STD for various strengths of random inter-group coupling through numerical simulation. We show that combining periodic mode permutation and mode scrambling reduces a link's GD STD by a factor of at least 3.13 compared to a link that relies solely on periodic mode scrambling. Finally, we perform numerical simulations to study how transverse and longitudinal index profile fabrication errors affect the mode permuter MAL and MDL STD and link GD STD.

The remainder of the paper is organized as follows. Section II describes an analytical method for computing the optimal mode permutation matrices given a fiber with specific mode groups and modal GDs. Section III describes the mode permuter structure based on cascaded LPFGs, modal propagation in LPFGs, the design of the mode permuter fiber transverse index profile, and the design of the grating transverse and longitudinal index profiles. Section IV details the two LPFG-based mode permuter designs, quantifies their performance, and evaluates the free-form-optimized mode permuter's efficacy in reducing the GD STD of a long-haul link. Sections V and VI are the discussion and conclusion, respectively.

II. Group Delay Management of MDM Links Using Mode Permutation

Prior studies have described mode permutation schemes for links supporting various numbers of modes [16], [17], [18], [19], [20], [21]. Since numerically evaluating link GD STD requires performing computationally intensive multi-section simulations [12], [24], [25], [26], [27], [40] or solving coupled stochastic differential equations [28], [41], [42], [43], [44], effective schemes are usually identified through non-exhaustive trial and error or heuristics [16], [17], [18], [19], [20], [21]. However, this approach becomes impractical as the number of modes increases. Using the analytical expressions described in [27], this section provides analytical formulas for evaluating the GD STD of self-compensated links employing a GI transmission fiber

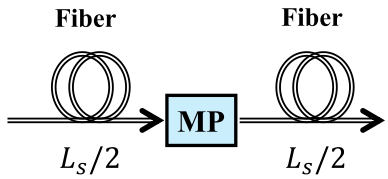

Fig. 1. Diagram of self-compensation. The mode permuter is placed in between two identical fiber segments of length $L_S/2$. MP: Mode Permuter.

with N_g mode groups and D spatial and polarization modes. We use this framework to find optimal self-compensation schemes, starting with the simple case of $N_g = 2$ mode groups and $D = 2$ modes, then progressing to $N_g = 3$ mode groups and $D = 12$ modes. In subsequent sections, we describe the design of a mode permuter for the latter case.

We consider a single span of a self-compensated link, shown in Fig. 1, employing a lossless, unitary mode permuter, described by a $D \times D$ transfer matrix $\boldsymbol{R}_{\text{MP}}$, between identical fiber segments of length $L_s/2$, where L_s is the length of the span. The D modes are grouped into N_g mode groups; the set of modes in the ith mode group is denoted by $\mathcal{M}_i$ and the degeneracy is given by $d_i = |\mathcal{M}_i|$, where $|\cdot|$ represents the cardinality. The mode group degeneracies are collected into an $N_g \times 1$ mode-group degeneracy vector $\mathbf{d} = [d_1, d_2, \ldots, d_{N_g}]^T$, where $(\cdot)^T$ denotes the transpose.

The $D \times D$ transfer matrix of the span is a product of transfer matrices:

$$\mathbf{M}_{\text{tot}}(\omega) = \mathbf{M}_2(\omega)\boldsymbol{R}_{\text{MP}}\mathbf{M}_1(\omega), \tag{1}$$

where the matrices $\mathbf{M}_1(\omega)$ and $\mathbf{M}_2(\omega)$ denote the $D \times D$ frequency-dependent random transfer matrices of the two fiber sections. From the total transfer matrix $\mathbf{M}_{\text{tot}}$, we evaluate the overall link GD STD using the GD operator [46], [47]

$$\mathbf{G} = -j\mathbf{M}_{\text{tot}}^{-1}(\omega)\frac{\partial \mathbf{M}_{\text{tot}}}{\partial \omega}, \tag{2}$$

where $j = \sqrt{-1}$. We note that (2) remains valid even in the presence of loss. The eigenvectors of $\mathbf{G}$ are the principal modes [46], and the eigenvalue of the mth principal mode, $\boldsymbol{\tau}_{\text{tot},i}$, represents its GD. Since we are only interested in the GD STD, we can remove the average GD from each principal mode so that $\sum_{i=1}^{D} \boldsymbol{\tau}_{\text{tot},i} = 0$. Therefore, the span GD STD can be written as

$$\sigma_{\text{GD}} = \sqrt{\frac{1}{D}\mathbb{E}\left\{\|\boldsymbol{\tau}_{\text{tot}}\|^2\right\}}, \tag{3}$$

where $\mathbb{E}\{\cdot\}$ denotes the expected value and $\|\cdot\|$ represents the Euclidean or l^2-norm.

Following the analysis in [27], we define a mode-group-averaged N_g-dimensional GD vector (measured in seconds) representing each of the transmission fiber segments. For mode group $i = 1, 2, \ldots, N_g$,

$$\tau_{0,i} = \frac{L_s/2}{d_i}\sum_{k \in \mathcal{M}_i} \beta_1[k],$$

where $\beta_1[k]$ is the uncoupled GD per unit length of the kth mode of the transmission fiber such that $\sum_{k=1}^{D} \beta_1[k] = 0$. The $N_g \times N_g$ mode-group power coupling matrix of the mode permuter is given by

$$\boldsymbol{\mathcal{P}}_{\text{MP}}[i,j] = \sum_{l \in \mathcal{M}_i}\sum_{m \in \mathcal{M}_j} |\boldsymbol{R}_{\text{MP}}[l,m]|^2,$$

The i, j element of $\boldsymbol{\mathcal{P}}_{\text{MP}}$ is the power the mode permuter transfers from M_i to M_j.

In the absence of random inter-group coupling, loss, and assuming a negligible intra-group GD STD, the span GD STD is given by [27, eq. (4)]

$$\mathbb{E}\left\{\|\boldsymbol{\tau}_{\text{tot}}\|^2\right\} = 2\boldsymbol{\tau}_0^H\mathbf{D}\boldsymbol{\tau}_0 + 2\boldsymbol{\tau}_0^H\boldsymbol{\mathcal{P}}_{\text{MP}}\boldsymbol{\tau}_0, \tag{4}$$

where $\mathbf{D}$ is the $N_g \times N_g$ diagonal matrix of mode group degeneracy, $\mathbf{D}[i,i] = d_i$. Since $\boldsymbol{R}_{\text{MP}}$ is a unitary matrix, the constraints on the entries of $\boldsymbol{\mathcal{P}}_{\text{MP}}$ are given by [27, eq. (13)]

$$\begin{aligned}
&\boldsymbol{\mathcal{P}}_{\text{MP}}[i,j] \geq 0,\ 1 \leq i \leq N_g,\ 1 \leq j \leq N_g,\\
&\mathbf{D}^{-1}\boldsymbol{\mathcal{P}}_{\text{MP}}\mathbf{1}_{N_g} = \mathbf{1}_{N_g},\\
&\mathbf{d}^T\mathbf{D}^{-1}\boldsymbol{\mathcal{P}}_{\text{MP}} = \mathbf{d}^T.
\end{aligned} \tag{5}$$

Here, $\mathbf{1}_{N_g}$ denotes the all-ones column vector of dimension N_g. For a specific $\boldsymbol{\tau}_0$, finding the optimal $\boldsymbol{\mathcal{P}}_{\text{MP}}$ to minimize (4) under the constraints in (5) is a convex optimization problem [27]. We obtain the optimal $\boldsymbol{\mathcal{P}}_{\text{MP}}$ for two combinations of N_g, D, and $\mathbf{d}$.

Case 1: $N_g = 2$, $D = 2$, and $\mathbf{d} = [1,1]^T$

First, we study the case of a link supporting two modes in different mode groups [1].

The two components of $\boldsymbol{\tau}_0$ are defined to be equal and opposite, $\tau_{0,1} = -\tau_{0,2}$, and the constraints in (5) reduce to

$$\begin{aligned}
&\boldsymbol{\mathcal{P}}_{\text{MP}}[i,j] \geq 0,\ 1 \leq i \leq 2,\ 1 \leq j \leq 2,\\
&\boldsymbol{\mathcal{P}}[1,1] + \boldsymbol{\mathcal{P}}[1,2] = \boldsymbol{\mathcal{P}}[1,1] + \boldsymbol{\mathcal{P}}[2,1] = 1,\\
&\boldsymbol{\mathcal{P}}[2,1] + \boldsymbol{\mathcal{P}}[2,2] = \boldsymbol{\mathcal{P}}[1,2] + \boldsymbol{\mathcal{P}}[2,2] = 1,
\end{aligned} \tag{6}$$

We find that $\mathbb{E}\{\|\boldsymbol{\tau}_{\text{tot}}\|^2\} = 0$ when $\boldsymbol{\mathcal{P}}_{\text{MP}}$ is equal to the exchange matrix $\mathbf{J}_2$:

$$\boldsymbol{\mathcal{P}}_{\text{MP}} = \mathbf{J}_2 = \begin{bmatrix} 0 & 1 \\ 1 & 0 \end{bmatrix}. \tag{7}$$

Intuitively, this result is expected since each signal travels equally in the slow and fast modes. Next, we examine a practical scenario in which varying mode-group degeneracies and uncoupled group delays complicate perfect group delay compensation.

Case 2: $N_g = 3$, $D = 12$, and $\mathbf{d} = [2,4,6]^T$

This case represents a link using a typical $D = 12$-mode GI transmission fiber with the following signal modes, each with two polarizations: $\{LP_{01}\}$, $\{LP_{11a}, LP_{11b}\}$, $\{LP_{02}, LP_{21a}, LP_{21b}\}$.

Minimizing (4) requires a specific combination of $\boldsymbol{\tau}_0$ and $\boldsymbol{\mathcal{P}}_{\text{MP}}$. We find that $\mathbb{E}\{\|\boldsymbol{\tau}_{\text{tot}}\|^2\} = 0$ when

$$\boldsymbol{\tau}_{0,1} = \boldsymbol{\tau}_{0,2} = -\boldsymbol{\tau}_{0,3}, \tag{8a}$$

[1]This example is purely mathematical and is not physically realizable in an axially symmetric fiber.

$$\boldsymbol{\mathcal{P}}_{\text{MP}} = \begin{bmatrix} 0 & 0 & 2 \\ 0 & 0 & 4 \\ 2 & 4 & 0 \end{bmatrix}. \tag{8b}$$

This combination of $\boldsymbol{\tau}_0$ and $\boldsymbol{\mathcal{P}}_{\text{MP}}$ requires the GDs of the first two mode groups to be equal and opposite to those of the third mode group, while the mode permuter must exchange all power between the third mode group and the first two mode groups. In the next section, we propose and design an LPFG-based mode permuter with the optimal mode-averaged power coupling matrix in (8b).

The self-compensation schemes outlined here ideally achieve total GD compensation, but their implementation is challenging due to unwanted inter-group coupling arising from link components, splicing, and manufacturing defects. This unwanted mode coupling hinders equal transmission of signals in both slow and fast modes, thereby compromising the GD STD reduction. These same issues also impact conventional GD compensation [44]. In Section IV, when assessing the performance of our designed mode permuters in a self-compensated link, we account for the influence of splicing, loss, and random inter-group coupling by employing standard multi-section simulation [11], [25], [31].

III. Mode Permuter Design Methodology

This section presents a methodology for the design of a $D = 12$-mode LPFG-based mode permuter that exchanges all power between the third mode group and the first two mode groups. We first describe the proposed mode permuter structure, comprised of a sequence of mode couplings performed by a cascade of gratings. Then, we describe our modeling methodology, the design of the mode permuter fiber transverse index profile, and the design of the grating transverse and logitudinal index profiles. In the following section, we employ this methodology to design LPFG-based mode permuters for a long-haul MDM system supporting $D = 12$ guided spatial and polarization modes, which we refer to as the signal modes.

We describe the mode permuter design methodology primarily with scalar, linearly polarized modes, making reference to vector modes when necessary. The term "mode permuter" hereafter refers to LPFG-based mode permuters unless noted otherwise.

To design the mode permuter and accurately assess its performance within an MDM link, a transmission fiber design is required. Although transmission fiber design is not the primary focus of this work, we briefly summarize the process here, with full details available in [45]. Following the approach in [48], a trench-assisted GI fiber is defined by multiple parameters, including core radius, relative index difference, graded-index exponent, and trench width. Numerical optimization is employed to identify a set of parameters that produces group delays satisfying the condition in (8a), while also maintaining sufficiently low bending losses.

Fig. 2 shows the resulting transverse index profile and normalized group delays of the transmission fiber. While the group delays are not ideal, the resulting fiber provides a realistic and practical design scenario. It can be verified that the $\boldsymbol{\mathcal{P}}_{\text{MP}}$ in (8b) remains optimal for self-compensation across the entire C-band for this fiber.

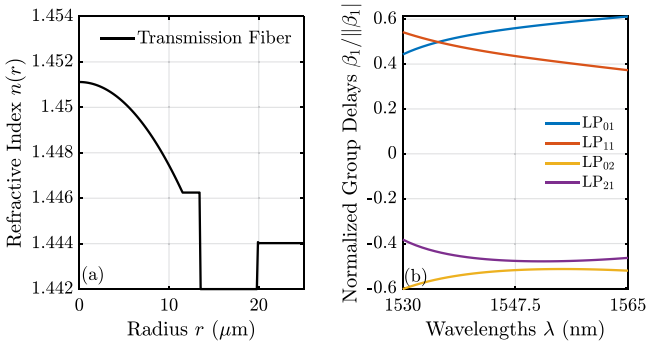

Fig. 2. (a) Transverse index profile and (b) normalized group delays of the six-spatial-mode transmission fiber designed for self-compensation.

A. Proposed Mode Permuter Structure

Numerous mode permutations can yield the optimal mode-group-summed power coupling matrix $\boldsymbol{\mathcal{P}}_{\text{MP}}$ in (8b). Due to differing mode field symmetries, exchanging power between LP_{01} and LP_{02} and between LP_{11} and LP_{21} is best. In the spatial mode basis $\{\text{LP}_{01}, \text{LP}_{11a}, \text{LP}_{11b}, \text{LP}_{02}, \text{LP}_{21a}, \text{LP}_{21b}\}$, the transfer matrix of these mode permutations is given by

$$\boldsymbol{R}_{\text{MP}} = \begin{bmatrix} 0 & 0 & 0 & \mathbf{1} & 0 & 0 \\ 0 & 0 & 0 & 0 & \mathbf{1} & 0 \\ 0 & 0 & 0 & 0 & 0 & \mathbf{1} \\ \mathbf{1} & 0 & 0 & 0 & 0 & 0 \\ 0 & \mathbf{1} & 0 & 0 & 0 & 0 \\ 0 & 0 & \mathbf{1} & 0 & 0 & 0 \end{bmatrix}. \tag{9}$$

Since only the power is relevant, the phase of each entry can be arbitrary as long as $\boldsymbol{R}_{\text{MP}}$ remains unitary. We note that while practical designs will not exactly achieve $\boldsymbol{R}_{\text{MP}}$, having imperfect mode conversion and loss, link GD STD can still be significantly reduced.

There are two approaches to obtaining this transfer matrix using cascaded gratings. One possibility is to cascade two gratings: $\{\text{LP}_{01}$–LP_{02}, LP_{11}–$\text{LP}_{21}\}$. Another possibility is to cascade four gratings: $\{\text{LP}_{01}$–LP_{11a}, LP_{11a}–LP_{02}, LP_{01}–LP_{11a}, LP_{11}–$\text{LP}_{21}\}$. In this case, the first three gratings perform the LP_{01} and LP_{02} power exchange by transferring power through LP_{11a}.

We considered both options and found that the four-grating cascade performs best. Although the two-grating cascade uses fewer gratings, the LP_{01}–LP_{02} grating necessitates a mode permuter fiber with a core-cladding index difference significantly larger than that of the transmission fiber to prevent the grating from also coupling the LP_{21} and LP_{02} modes into unguided modes. The four-grating cascade solely transfers power between modes of adjacent mode groups, so the core-cladding index difference can be lower. As a result, the splicing loss between the mode permuter fiber and the transmission fiber is significantly

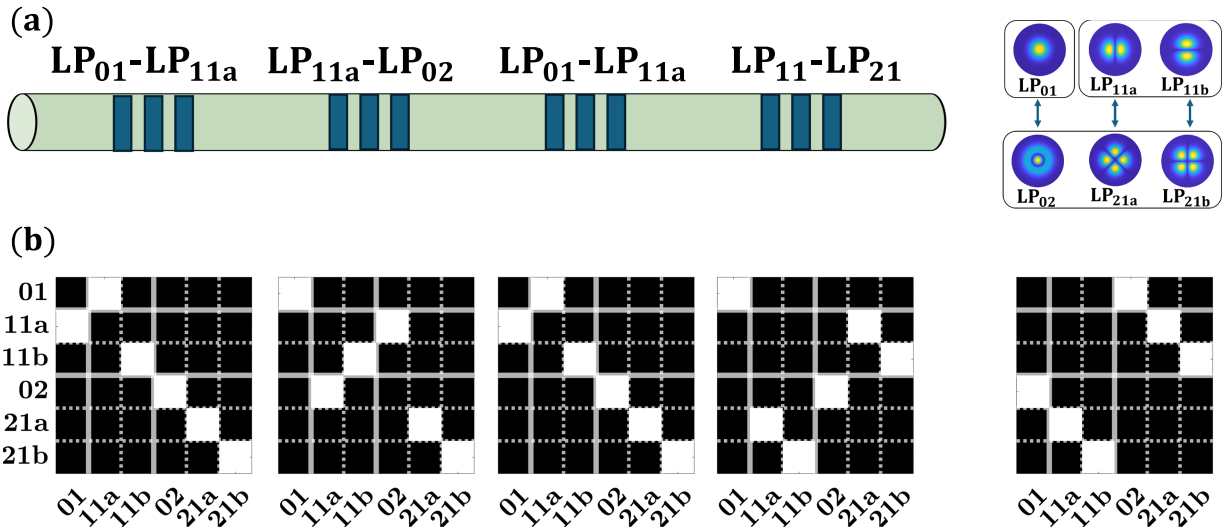

Fig. 3. (a) Principal structure of the mode permuter, comprised of four cascaded LPFGs, and the resulting mode exchanges. (b) The transfer matrices of the individual gratings and the mode permuter, shown in the basis of LP spatial modes. The first three gratings exchange LP_{01} and LP_{02} with LP_{11a} as an intermediate stage. The final grating exchanges LP_{11} and LP_{21}.

lower for the four-grating cascade than for the two-grating cascade. One disadvantage of the four-grating cascade is that the efficiencies of the LP_{01}–LP_{11a} and LP_{11a}–LP_{02} mode conversions are degraded by the instability of the $\mathrm{LP}_{11a,x}$ and $\mathrm{LP}_{11a,y}$ modes, which periodically convert to $\mathrm{LP}_{11b,y}$ and $\mathrm{LP}_{11b,x}$, respectively, according to the beat lengths of the $\mathrm{TE}_{01}/\mathrm{HE}_{21}$ and $\mathrm{TM}_{01}/\mathrm{HE}_{21}$ vector mode pairs that compose the LP_{11} modes [34], [35], [49]. Although this impairs the mode conversion efficiency, we find that the reduced splicing loss is a preferable trade-off.

Fig. 3 illustrates the key components of the proposed mode permuter, consisting of four cascaded LPFGs. The first three gratings facilitate the exchange between LP_{01} and LP_{02}, using LP_{11a} as an intermediate state. The last grating exchanges both LP_{11} modes with both LP_{21} modes. The ideal transfer matrices for the individual gratings, as well as their combination, are shown in the basis of LP spatial modes.

To implement the proposed mode permuter, we must design three distinct gratings: LP_{01}–LP_{11a}, LP_{11a}–LP_{02}, and LP_{11}–LP_{21}. We limit our designs to those using the same fiber for all gratings to reduce the number of splices needed. This choice makes designing the mode permuter fiber's transverse index profile more challenging, yet simplifies its fabrication.

B. Modeling Methodology

The total refractive index (RI) for each of the gratings in the mode permuter can be written as

$$n_{\mathrm{tot}}(r,\theta,z) = n(r) + \Delta n_{\mathrm{g}}(r,\theta)\left(1+\cos\left(\frac{2\pi z}{\Lambda}+\phi(z)\right)\right) \tag{10}$$

where $n(r)$ is the mode permuter fiber's transverse index profile, $\Delta n_{\mathrm{g}}(r,\theta)$ is the grating transverse index profile change induced by single- or multi-sided UV illumination, and $\phi(z)$ is the longitudinal chirp profile. $n(r)$ is not necessarily the same as the transverse index profile of the transmission fiber $n_{\mathrm{init}}(r)$. We assume the index modulation induced by single-sided UV exposure is present only in the fiber core region and follows a decreasing exponential function, where it is given by

$$\Delta n_{\mathrm{ss}}(r,\theta;\psi) = \chi \exp\left[-\rho\left(\sqrt{r_{\mathrm{core}}^2 - r^2\sin^2(\theta-\psi)} - r\cos(\theta-\psi)\right)\right]P(r) \tag{11}$$

where χ is the modulation depth, ρ is the exponential decay rate of the index modulation, r_{core} is the core radius, ψ is the azimuthal angle of the UV illumination, and $P(r)$ is the radial dependence of the index modulation [50], [51]. Here, $P(r)=1$ within the core and $P(r)=0$ outside the core. For a single-sided UV grating, $\Delta n_{\mathrm{g}} = \Delta n_{\mathrm{ss}}$. Fig. 4 shows the normalized refractive index change due to a single-sided UV illumination with

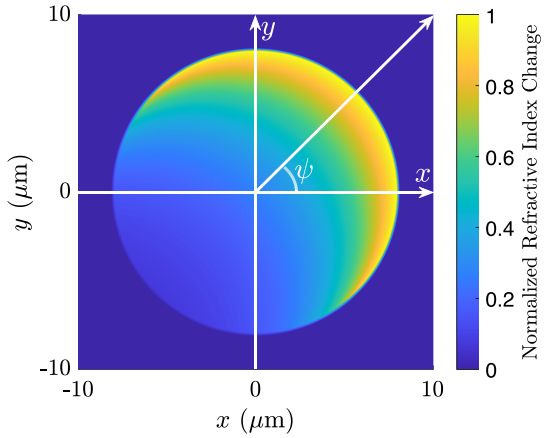

Fig. 4. Normalized refractive index change due to single-sided UV illumination with an illumination angle of $\psi = \pi/4$.

$\psi = \pi/4$. The grating transverse index profile is directional and axially asymmetric, enabling coupling of modes with differing angular symmetries [50].

The coupled-mode propagation equations describe the propagation of both guided and unguided modes in the mode permuter and can be solved to obtain $\boldsymbol{R}_{\text{MP}}$ [31], [50], [51]. The guided and unguided mode fields and propagation constants $\boldsymbol{\beta}$ are computed in a radially resolved cylindrical geometry with a perfectly matched layer and zero termination boundary condition, as in [31], [51]. We assume the outer cladding is index-matched to the inner cladding, which can be achieved with an index-matched coating [52]; thus, no discrete cladding modes are supported [31] and inner-outer cladding reflections are suppressed [52]. Loss in $\boldsymbol{R}_{\text{MP}}$ arises from undesired coupling between guided signal modes and unguided modes or guided non-signal modes during the permutation process. We also consider loss and coupling from modal field mismatches between the modes in the transmission fiber and those in the mode permuter, which are referred to as splicing losses [53]. Combining all these effects, we can evaluate the mode permuter MDL STD and MAL using the modal gain operator [12].

C. Mode Permuter Fiber Transverse Index Design

In this subsection, we first explain key constraints for the modal propagation constants of the mode permuter fiber. We then explain how to design an SI fiber that satisfies these constraints and how to use free-form index optimization to obtain an improved design.

1) Working Principle of LPFGs: Mode coupling by an LPFG is a coherent, phase-matched process [31], [40], [50]. A uniform grating couples two modes most efficiently when

$$\Delta\beta = \frac{2\pi}{\Lambda}, \tag{12}$$

where the propagation constant spacing $\Delta\beta$ is the difference between the modal propagation constants and Λ is the grating period. Considering a simple case in which an MMF supports only two modes, we can evaluate the maximum coupling efficiency η between the modes achievable by a grating:

$$\eta \approx \frac{1}{1 + \left(\frac{\Delta\beta - 2\pi/\Lambda}{\kappa}\right)^2}, \tag{13}$$

where κ is the coupling coefficient between the two modes induced by the grating and the self-coupling coefficients are assumed to be negligible [50]. The grating length for greatest power transfer occurs at length

$$L_c = \frac{\pi}{2|\kappa|}.$$

For coupling between mode i, LP_{lm}, and mode j, $\text{LP}_{l'm'}$, we denote the propagation constant spacing as:

$$\Delta\beta_{lm,l'm'} = |\beta[i] - \beta[j]|.$$

2) Design Criterion: Mode permutation relies on controlled, complete power exchanges between particular pairs of modes. To achieve this, we require the $D = 12$ mode permuter fiber to satisfy the following design criterion:

C.1 The propagation constant spacings of the desired mode exchanges LP_{01}–LP_{11}, LP_{11}–LP_{02}, and LP_{11}–LP_{21} must be well separated from each other and from every spacing between a signal mode and any other signal, guided non-signal, or unguided mode.

If this design criterion is satisfied, the LP_{01}–LP_{11a}, LP_{11a}–LP_{02}, and LP_{11}–LP_{21} gratings can be inscribed in the same mode permuter fiber, each performing their desired mode exchanges with high coupling efficiency while exhibiting low loss and minimal unwanted coupling.

3) Choice of Mode Permuter Fiber: A GI-MMF, which has been suggested for mode scramblers [11], [31], [40] or long-haul transmission fibers [7], [16], [54], is inadequate for our proposed mode permuter. This inadequacy arises because the propagation constant spacings between modes of adjacent mode groups are nearly identical, and the LP_{02} and LP_{21} modes are nearly degenerate [11]. As a result, it becomes impossible to couple specific pairs of modes without unintentionally coupling others. In contrast, SI-MMFs do not have these properties and thus are a more suitable option.

Fig. 5 illustrates an exemplary SI transverse index profile with propagation constants and propagation constant spacings that satisfy the design criterion C.1. Fig. 5(a) shows the SI transverse index profile. Fig. 5(b) and (c) show the propagation constants and the corresponding propagation constant spacings, respectively. In Fig. 5(c), the spacings of desired mode transitions, identified in C.1, are in blue while all others are in gray. Visually, design criterion C.1 requires that the propagation constant spacings of the desired transitions (blue) are not near each other or other transitions (gray).

We consider two transverse index profile designs. In the first design, we restrict ourselves to SI profiles. In the second design, we use free-form index optimization from [55] to find an improved design. For both fibers, we follow two objectives to guide our design process. Firstly, we want to minimize the MAL and MDL STD from splicing between the transmission fiber and the mode permuter fiber to reduce device loss. Secondly, we want to maximize the separation between the desired transitions and adjacent transitions to minimize unwanted coupling to guided or unguided modes.

4) Step-Index Profile Optimization: For the SI design, we only need to find a combination of core radius r_{core} and relative index difference Δ. We define a transition separation metric, which quantifies how well-separated the LP_{01}–LP_{11}, LP_{11}–LP_{02}, and LP_{11}–LP_{21} transitions are from other transitions. It is evaluated by the following formula:

$$\begin{aligned}\Delta\beta_{\text{ts}} = \\ \min\Bigg\{ &\min_{(lm,l'm')\notin\{(01,11),(02,31)\}} \{|\Delta\beta_{01,11} - \Delta\beta_{lm,l'm'}|\}, \\ &\min_{(lm,l'm')\notin\{(11,02),(02,31)\}} \{|\Delta\beta_{11,02} - \Delta\beta_{lm,l'm'}|\}, \\ &\min_{(lm,l'm')\notin\{(11,21),(02,31)\}} \{|\Delta\beta_{11,21} - \Delta\beta_{lm,l'm'}|\}\Bigg\}.\end{aligned} \tag{14}$$

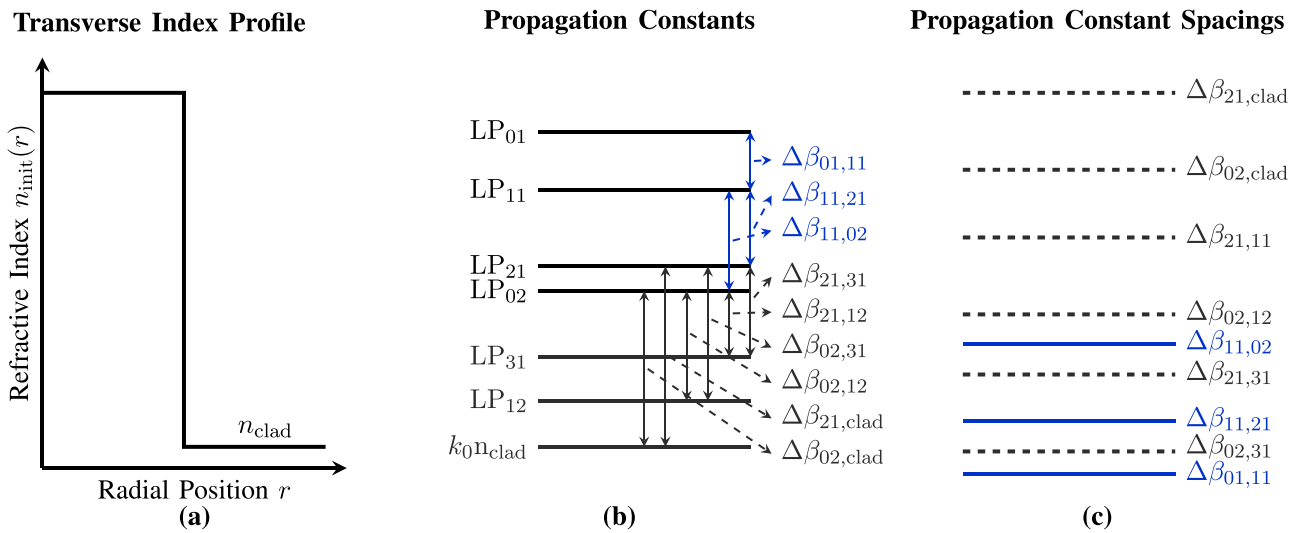

Fig. 5. Example of an SI fiber suitable for the mode permuter described in Section III-A: (a) transverse index profile, (b) propagation constants and (c) propagation constant spacings between modes in adjacent mode groups. In (b), guided modes not used for signal propagation and the cladding index are in gray. In (b) and (c), propagation constant spacings for the LP_{01}–LP_{11}, LP_{11}–LP_{02}, and LP_{11}–LP_{21} transitions are in blue, while all others are dashed and gray.

In the evaluation of $\Delta\beta_{\text{ts}}$, we exclude the inefficient LP_{02}–LP_{31} transition, as its coupling coefficient is an order of magnitude smaller than those of other transitions for the UV illuminations we use.[2]

We search for designs that have a transition separation $\Delta\beta_{\text{ts}}$ of over 800 m^{-1}, which we find is sufficient to suppress unwanted mode coupling. A separation of only 100 m^{-1} is sufficient to effectively suppress this mode exchange. From these designs, we select a design with the lowest MDL STD and MAL.

5) Free-Form Index Optimization: We perform free-form optimization to design a fiber that is an improvement from the SI fiber in two regards, the first being lower MDL and MAL when splicing to and from the transmission fiber. To that end, the transmission fiber is used as the initial design that is perturbed to achieve the final mode permuter fiber.

The second objective is to further separate the propagation constant spacings of the desired transitions from all other spacings to limit any unwanted coupling. Since the SI fiber is much closer to meeting this objective than the transmission fiber, the SI fiber is the target in the first optimization phase.

We use the propagation constant engineering method described in [55]. The objective function is a weighted sum of the squared differences between the actual propagation constants $\boldsymbol{\beta}$ and target propagation constants $\boldsymbol{\beta}^{\text{tar}}$:

$$J = \sum_{i \in \mathcal{M}_{\text{guided}}} w_i \left(\beta_i - \beta_i^{\text{tar}}\right)^2, \tag{15}$$

where $\mathcal{M}_{\text{guided}}$ is the set of guided mode indices and w_i is the weighting placed on mode i. The weighting parameter is determined heuristically for each phase of the optimization, with greater emphasis placed on modes involved in transitions that are more challenging to space apart from others. We use gradient descent to iteratively update the transverse index profile at each radial coordinate r as

$$n(r) \leftarrow n(r) - \mu \frac{\partial J}{\partial n(r)}, \tag{16}$$

where μ is a step-size parameter that is chosen sufficiently small that perturbative modeling is valid. Details on computing the derivative $\frac{\partial J}{\partial n(r)}$ can be found in [55].

In subsequent optimization phases, the design is further improved by making the target propagation constants more idealized than those of the SI fiber, allowing the new design to surpass its performance. The target spacings are spread apart further and, in some phases, strategically rearranged to create more separation from the desired transitions. Multiple optimization phases, each targeting specific transitions, help ensure the design is maximally optimized. These additional phases continue to fine-tune the target spacings until the desired transitions are sufficiently isolated.

The optimization process features a tradeoff between maintaining low splicing loss and achieving a large separation between desired and undesired transitions. Perturbations to the RI profile must remain subdued to limit the loss from splicing between the mode permuter and the transmission fiber. Meanwhile, the transmission fiber's equally spaced propagation constants must be changed rather dramatically to overcome the inadequacies enumerated in Section III-C3.

D. Grating Transverse and Longitudinal Index Design

This subsection describes the design of the transverse and longitudinal index profiles of the LP_{01}–LP_{11a}, LP_{11a}–LP_{02}, and LP_{11}–LP_{21} gratings.

Given a transverse index profile with propagation constant spacings satisfying design criterion C.1, the design of each grating follows the same phase-matching principles relevant to the design of low-loss and large bandwidth LPFG-based mode

[2]The coupling coefficient is weak primarily because of the large mismatch in mode angular symmetries.

TABLE I
COUPLING COEFFICIENTS FOR SINGLE-SIDED AND DOUBLE-SIDED UV ILLUMINATION

Transitions	LP_{01}–LP_{11a}	LP_{01}–LP_{11b}	LP_{11a}–LP_{02}	LP_{11b}–LP_{02}	LP_{11a}–LP_{21a}	LP_{11b}–LP_{21b}	LP_{11a}–LP_{21b}	LP_{11b}–LP_{21a}
Single-sided $\chi = 15 \times 10^{-5}$, $\psi = 0$	43.1	0	32.0	0	35.6	40.5	0	0
Double-sided $\chi = 15 \times 10^{-5}$, $\psi = \pm\frac{\pi}{6}$	37.3	0	27.7	0	32.9	32.9	0	0

The coupling coefficients between select signal modes induced by single- or double-sided UV illumination. Some coupling coefficients are exactly 0 due to the symmetries of the modes and the grating transverse index profile.

converters described in references [33], [34], [35], [37]. We restrict ourselves to chirped, sinusoidal gratings described by (10). We assume that the transverse index perturbation induced by a single-sided UV illumination is given by (11). Each grating will be inscribed with one or more UV illuminations. Therefore, for each grating we need to determine the transverse index profile and grating parameters: modulation depth χ, UV illumination angle(s) ψ, grating period Λ, grating length L_g, and chirp profile $\phi(z)$.

1) Grating Transverse Index Profile: First, we determine the transverse index profile for each of the gratings. The LP_{01}–LP_{11a} and LP_{11a}–LP_{02} gratings involve coupling an axially symmetric LP mode LP_{0m} to the axially asymmetric LP_{11a}. Since the transverse perturbation induced by a single-sided UV illumination is directional and axially asymmetric, we can independently couple LP_{01} or LP_{02} to the a or b modes of LP_{11} by setting the UV illumination angle ψ to 0 or $\frac{\pi}{2}$, respectively. A single-sided grating is not suitable for exchanging all power between LP_{11a}–LP_{21a} and LP_{11b}–LP_{21b} because its transverse index profile results in unequal coupling coefficients for those pairs of modes [34], [35]. We can resolve this issue by using double-sided UV illumination [35]. We find that a double-sided UV illumination at angles $\psi = \frac{\pi}{6}$ and $\psi = -\frac{\pi}{6}$ and identical modulation depths will equalize those coupling coefficients. In this case, the transverse index perturbation is given by

$$\Delta n_{\text{ds}}(r,\theta) = \Delta n_{\text{ss}}\left(r,\theta;\psi=\frac{\pi}{6}\right) + \Delta n_{\text{ss}}\left(r,\theta;\psi=-\frac{\pi}{6}\right) \tag{17}$$

Table I shows the coupling coefficients κ between the LP_{01} and LP_{11} modes, LP_{02} and LP_{11} modes, and LP_{11} and LP_{21} modes for a single-sided UV illumination grating described by $\Delta n_{\text{ss}}(r,\theta;\psi=0)$ and a double-sided UV illumination described by $\Delta n_{\text{ds}}(r,\theta)$. The single-sided illumination uses a modulation depth of $\chi = 15 \times 10^{-5}$, while the double-sided illumination uses a modulation depth of $\chi = 7.5 \times 10^{-5}$. Some coupling coefficients are exactly 0 due to the symmetries of the modes and the UV illumination transverse profile.

Table I verifies that a single-sided illumination can couple LP_{01} or LP_{02} to LP_{11a} without simultaneously coupling to LP_{11b} and is therefore suitable for the LP_{01}–LP_{11a} and LP_{11a}–LP_{02} gratings. Performing these couplings with a double-sided illumination offers no advantage. We also confirm that a single-sided illumination induces unequal coupling coefficients between LP_{11a}–LP_{21a} and LP_{11b}–LP_{21b}, while the double-sided UV illumination in (17) equalizes those coupling coefficients. Hence, we will use single-sided illumination for the LP_{01}–LP_{11a} and LP_{11a}–LP_{02} gratings and double-sided illumination for the LP_{11}–LP_{21} grating.

A double-sided UV illumination can be carried out as described in [35], by setting the UV laser direction fixed and using rotatable fiber clamps.

2) Grating Longitudinal Index Profile: We now outline the design of the grating longitudinal profile. A linearly chirped grating is suitable for achieving high coupling efficiency across the entire C-band, as it offers greater bandwidth than a uniform grating due to enhanced phasematching. The design of linearly chirped mode converters has been described in [56].

Following [56], we use a linear chirp profile given by

$$\phi(z) = \frac{\alpha z^2}{2L_c^2}. \tag{18}$$

where α is the chirp parameter. Therefore, the grating period changes along the grating's length and is expressed by

$$\frac{1}{\Lambda(z)} = \frac{1}{\Lambda_0} - \frac{\alpha z}{2\pi L_c^2}, \tag{19}$$

where Λ_0 is the grating period at $z = 0$. Depending on the chirp parameter α, there is an optimal grating length L_g for high bandwidth mode conversion, which has been detailed in [56]. For maximum coupling efficiency at the center wavelength λ_0, Λ_0 can be evaluated by

$$\frac{1}{\Lambda_0} = \frac{\Delta\beta_{lm,l'm'}(\lambda_0)}{2\pi} + \frac{\alpha L_g}{4\pi L_c^2}. \tag{20}$$

Finally, the modulation depth χ can be adjusted to meet coupling efficiency targets.

IV. RESULTS

In this section, we apply our proposed design strategy to design two LPFG-based mode permuters for a long-haul MDM link that supports $D = 12$ spatial and polarization modes. One design uses an SI transverse index profile for the mode permuter fiber, while the other uses a free-form-optimized profile. Finally, we evaluate the GD STD of a free-form-optimized mode permuter in a long-haul MDM link employing self-compensation. All values that depend on wavelength are provided over the C-band unless stated otherwise.

A. Design Case 1: Step-Index Fiber

Following the methodology in Section III, we design a mode permuter with gratings inscribed on an SI-MMF. We find the optimal core radius and relative index difference using a grid search. The core radius r_{core} is varied between 9.5 μm and

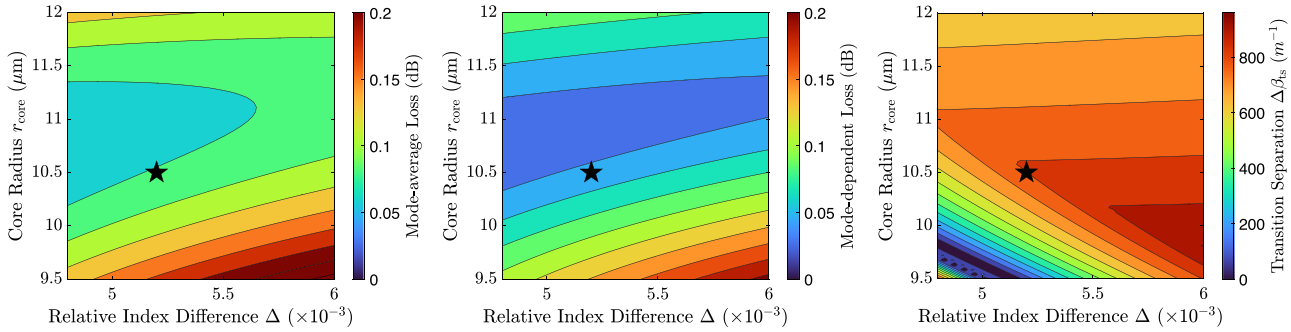

Fig. 6. Optimization of the step-index fiber: (a) MAL, (b) MDL, and (c) transition separation $\Delta\beta_{\text{ts}}$ as a function of relative index difference Δ and core radius r_{core} at 1550nm. The dark star indicates the chosen step-index fiber design.

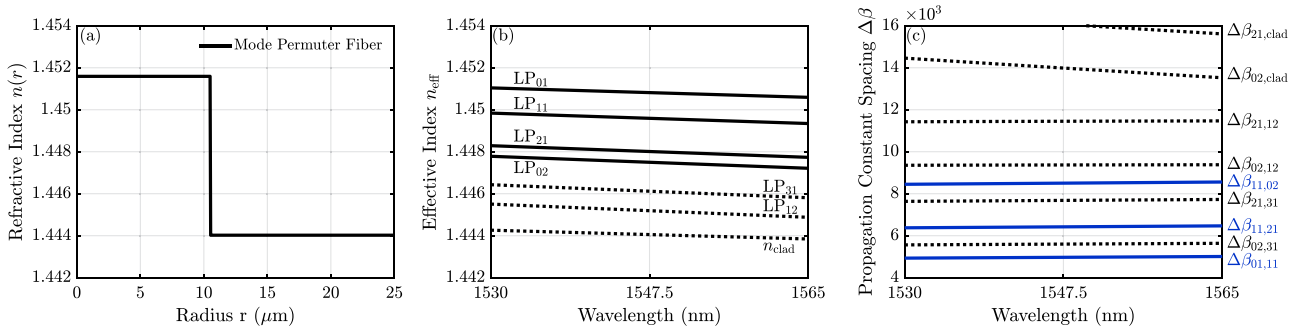

Fig. 7. SI-fiber mode permuter: (a) Transverse index profile, (b) guided mode effective indices and cladding index as a function of wavelength, and (c) select propagation constant spacings as a function of wavelength. In (b), guided modes not used for signal propagation and the cladding index are dashed. In (c), propagation constant spacings for the LP_{01}–LP_{11a}, LP_{11a}–LP_{02}, and LP_{11}–LP_{21} transitions are in blue, while all others are dashed.

12 μm, while the relative index difference Δ is varied between 0.46% and 0.6%. Each design is evaluated for splicing loss to the transmission fiber and separation of the LP_{01}–LP_{11}, LP_{11}–LP_{02}, and LP_{11}–LP_{21} transitions from other transitions.

Fig. 6 illustrates the splicing MAL, MDL STD, and transition separation $\Delta\beta_{\text{ts}}$. Fig. 6(a) and (b) show that MAL and MDL STD tend to be smallest for r_{core} between 10.5 and 11 μm and Δ between 0.46% and 0.56%. Fig. 6(c) indicates that the transition separation $\Delta\beta_{\text{ts}}$ exceeds 800 m^{-1} within a roughly triangular region, colored in dark orange, where the r_{core} less than 10.6 μm. We observe a tradeoff that challenges an SI fiber's ability to simultaneously minimize splicing-induced MAL and MDL STD while also maximizing the transition separation $\Delta\beta_{\text{ts}}$. We find that the SI fiber parameters $r_{\text{core}} = 10.5$ μm and $\Delta = 0.52\%$, indicated by a star in Fig. 6, achieve the best balance between low splicing loss and a high transition separation.

Fig. 7 illustrates the optimized SI fiber's transverse index profile, effective indices, and propagation constant spacings. The splicing MAL and MDL STD are under 0.08 dB and 0.05 dB, respectively. The propagation constant spacings $\Delta\beta_{01,11}$, $\Delta\beta_{11,02}$, and $\Delta\beta_{11,21}$ vary over wavelength by 77.5 m^{-1}, 109.3 m^{-1}, and 91.8 m^{-1}, respectively. The separations between the LP_{01}–LP_{11}, LP_{11}–LP_{02}, and LP_{11}–LP_{21} transitions and adjacent transitions are greater than 800 m^{-1}, excluding the inefficient LP_{02}–LP_{31} transition. The beat lengths of the $\text{TE}_{01}/\text{HE}_{21}$ and $\text{TM}_{01}/\text{HE}_{21}$ vector modes, which compose the $\text{LP}_{11a,x}$ and $\text{LP}_{11a,y}$ modes, are about 0.53 m and 1.23 m, respectively.

TABLE II
GRATING PARAMETERS FOR STEP-INDEX FIBER

Grating	LP_{01}–LP_{11a}	LP_{11a}–LP_{02}	LP_{11}–LP_{21}
UV Illumination Type	Single	Single	Double
UV Illumination Angle(s) ψ	0	0	$\pi/6$ and $-\pi/6$
Modulation Depth χ	40×10^{-5}	30×10^{-5}	10×10^{-5}
Grating Period Λ (μm)	1181.1	717.6	948.5
Grating Length L_g (cm)	2.75	5.01	7.29
Chirp Parameter α	4	4	4

The LP_{01}–LP_{11a}, LP_{11a}–LP_{02}, and LP_{11}–LP_{21} gratings are designed according to to the procedure in Section III-D. Table II provides the UV illumination type, UV illumination angle(s), and values of the modulation depth χ, grating period Λ, grating length L_g, and chirp parameter α for the LP_{01}–LP_{11a}, LP_{11a}–LP_{02}, and LP_{11}–LP_{21} gratings designed using the SI fiber. All gratings have a chirp parameter $\alpha = 4$ to increase coupling efficiency over the C-band. The initial grating period Λ_0 is set according to (20) with a center wavelength $\lambda_0 = 1547.5$ nm. The modulation depth of each grating is varied to obtain C-band coupling efficiency of over 97% while keeping MAL below 0.1 dB.

Fig. 8 shows the performance of the individual gratings, mode permuter, and mode permuter including splicing. Fig. 8(a) and (f)

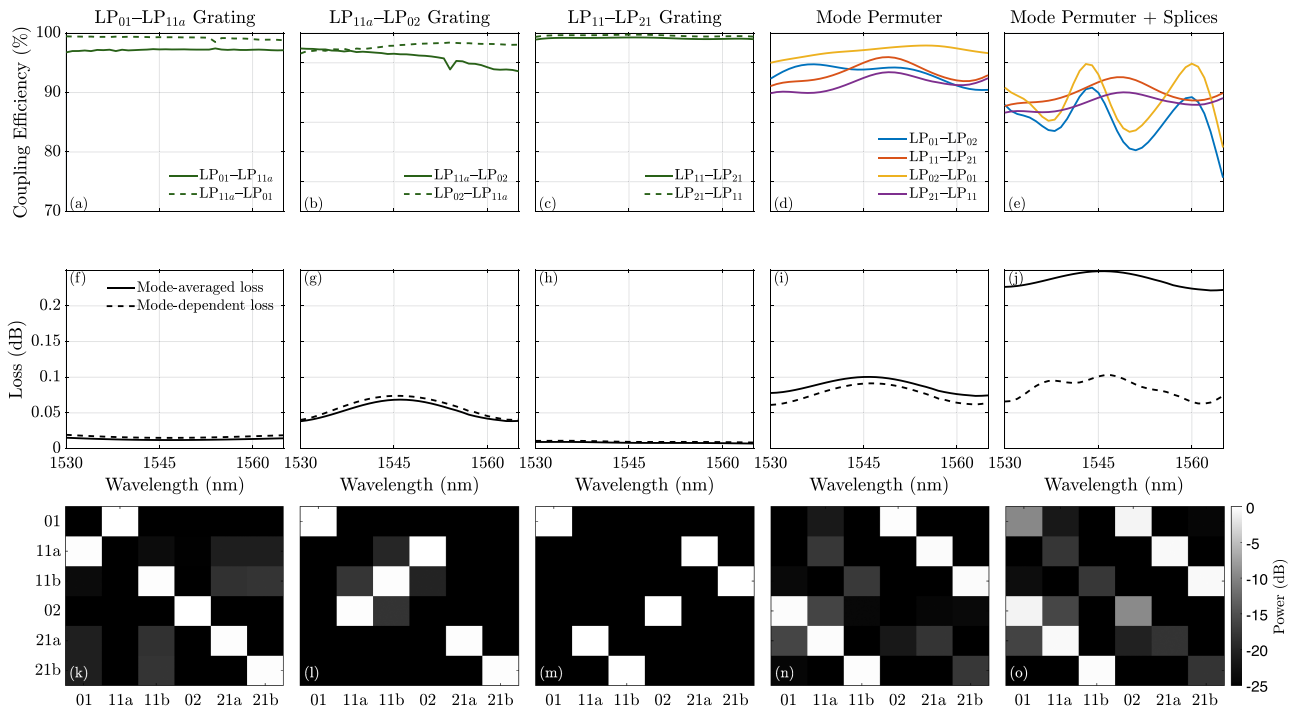

Fig. 8. Performance of the individual gratings and the mode permuter designed using the SI transverse index profile in Fig. 7. Transmission (a-e) and MAL and MDL (f-j) as a function of wavelength over the C-band of the (a, f) LP_{01}–LP_{11a} grating, (b, g) LP_{11a}–LP_{02}, (c, h) LP_{11}–LP_{21} grating, (d, i) mode permuter, and (e, j) mode permuter including splicing. Power coupling matrices (k-o) at 1550nm of the (k) LP_{01}–LP_{11a} grating, (l) LP_{11a}–LP_{02} grating, (m) LP_{11}–LP_{21} grating, (n) mode permuter, and (o) mode permuter including splicing.

show the LP_{01}–LP_{11a} coupling efficiency and MDL STD and MAL, respectively, of the LP_{01}–LP_{11a} grating. Coupling efficiency exceeds 97%, while the MAL and MDL STD are under 0.03 dB and 0.02 dB, respectively. Fig. 8(k) shows the power coupling matrix at 1550 nm. Less than -15 dB of unwanted power coupling from LP_{01} and LP_{11a} into LP_{11b}, LP_{21a}, and LP_{21b} is observed. This unwanted coupling occurs because the LP_{11}–LP_{21} transition is near the LP_{01}–LP_{11} transition.

Fig. 8(b) and (g) show the coupling efficiency and losses, respectively, of the LP_{11a}–LP_{02} grating. Coupling efficiency exceeds 94%, while the MAL and MDL STD are both under 0.07 dB. Fig. 8(l) shows the power coupling matrix at 1550 nm. Unwanted mode coupling to LP_{11b} occurs due to the instability of the $LP_{11a,x}$ and $LP_{11a,y}$ modes, which periodically convert to $LP_{11b,y}$ and $LP_{11b,x}$, respectively.

Fig. 8(c) and (h) show the coupling efficiency and losses, respectively, of the LP_{11}–LP_{21} grating. The reported coupling efficiencies are an average of the LP_{11a}–LP_{21a} and LP_{11b}–LP_{21b} coupling efficiencies. Coupling efficiency exceeds 99%, while the MAL and MDL STD are under 0.02 dB and 0.02 dB, respectively. Fig. 8(m) shows the power coupling matrix at 1550 nm. We observe less than -25 dB of unwanted mode coupling.

Compared to the LP_{01}–LP_{11a} and LP_{11}–LP_{21} gratings, the LP_{11a}–LP_{02} grating has substantially larger losses. This occurs since the LP_{11}–LP_{02} transition is near two undesired transitions with large coupling coefficients, LP_{11}–LP_{21} and LP_{21}–LP_{31}, while the LP_{01}–LP_{11} and LP_{11}–LP_{21} transitions are closest to the LP_{02}–LP_{31} transition, which has a very low coupling coefficient. In the next subsection, we use free-form index optimization to address this issue.

Fig. 8(d) and (i) show the mode permuter's coupling efficiencies and losses, respectively. The coupling efficiencies of the LP_{01}–LP_{02}, LP_{11}–LP_{21}, LP_{02}–LP_{01}, and LP_{21}–LP_{11} transitions exceed 89%, while the MAL and MDL STD are under 0.10 dB and 0.09 dB, respectively. Fig. 8(n) shows the power coupling matrix at 1550 nm. Unwanted mode coupling and imperfect mode conversion result in an imperfect albeit still effective mode permuter power coupling matrix.

Fig. 8(e) and (j) show the mode permuter's coupling efficiencies and losses, respectively, when including splicing to and from the transmission fiber. The coupling efficiencies of the LP_{11}–LP_{21} and LP_{21}–LP_{11} couplings exceed 86%, while those of the LP_{01}–LP_{02} and LP_{02}–LP_{01} couplings only exceed 76%. The degradation of the LP_{01}–LP_{02} mode exchange is from splicing, which causes additional, unwanted coupling between the LP_{01} and LP_{02} modes. At 1565 nm, efficiencies of the LP_{01}–LP_{02} and LP_{02}–LP_{01} couplings decrease by approximately 16%. Additionally, the MAL rises by 0.15 dB, whereas the MDL shows only a slight increase because the mode permuter compensates for the MDL created by the two splices. Fig. 8(o) shows the power coupling matrix at 1550 nm. The reduced coupling efficiency between LP_{01}–LP_{02} is clearly visible.

We have shown that a mode permuter with an SI-fiber can perform the desired mode permutations with relatively high coupling efficiency and low loss. However, splicing loss, undesired coupling between LP_{01} and LP_{02} from splicing, and

LP_{11a}–LP_{02} grating loss are key performance limiters. In the subsequent design case, we use free-form index optimization to address these issues and design a mode permuter with enhanced performance.

B. Design Case 2: Free-Form-Optimized Fiber

Following the methodology in Section III, we design an improved mode permuter fiber with free-form index optimization. The process consists of four phases, each with a different number of iterations N, weighting vector $\boldsymbol{w}$, step size μ, and set of target propagation constants $\{\boldsymbol{\beta}^{\text{tar}}[l\,m]\}$ over all guided modes LP_{lm}.

Phase 1: Starting with the transmission fiber as the initial state, we perform N_1 iterations with

$$\boldsymbol{\beta}^{\text{tar}} = \boldsymbol{\beta}^{\text{SI}}$$

for all guided modes, where $\boldsymbol{\beta}^{\text{SI}}$ are the propagation constants of the SI-MMF in Fig. 7.

Phase 2: We perform N_2 iterations where

$$\boldsymbol{\beta}^{\text{tar}}[02] = \boldsymbol{\beta}^{\text{SI}}[02] - \delta.$$

and the rest of the $\boldsymbol{\beta}^{\text{tar}}$ are identical to $\boldsymbol{\beta}^{\text{SI}}$. In the SI fiber, the LP_{11}–LP_{02} transition is close to the transitions adjacent to it on each side, causing some undesired coupling. Phase 2 rectifies this in the optimized design by shifting the LP_{02} mode downwards and thus reordering the spacings to create more separation from the LP_{11}–LP_{02} transition. This slight modification increases the separation between the LP_{11}–LP_{02} transition and all adjacent transitions by 50%, substantially reducing parasitic coupling.

Phase 3: We perform N_3 iterations where

$$\boldsymbol{\beta}^{\text{tar}}[11] = \boldsymbol{\beta}^{\text{SI}}[11] + \delta,$$
$$\boldsymbol{\beta}^{\text{tar}}[21] = \boldsymbol{\beta}^{\text{SI}}[21] + \delta.$$

and the rest of the $\boldsymbol{\beta}^{\text{tar}}$ are identical to $\boldsymbol{\beta}^{\text{SI}}$. This shifts LP_{11} and LP_{21} upwards, further separating all couplings and isolating the desired transitions.

Phase 4: The last stage of fine-tuning consists of N_4 iterations with the $\{\boldsymbol{\beta}^{\text{tar}}\}$ identical to those in Phase 3, but with the weightings changed to target undesired transitions that continue to interfere with the ideal permutation scheme. More iterations would isolate the desired transitions even further, but the additional RI perturbations cause more splicing loss. We select the value of n_4 to reflect the best compromise.

After sweeping each hyperparameter, we set $\delta = 6k_0 \times 10^{-4}$, $N_1 = 250$, $N_2 = 40$, $N_3 = 25$, and $N_4 = 15$. The step size μ is 5×10^{-6} for Phases 1-3 and is halved in Phase 4. The weighting w is increased by a factor of 4 for the particular mode or modes targeted in each phase and by a factor of 2 for the guided non-signal modes. It is important to note that the free-form optimization presented here includes significant trial and error and does not constitute a generalizable design approach. Due to the vast parameter space associated with free-form fibers and the large number of potential mode transitions that must be accounted for, developing a systematic and exhaustive design methodology, similar to that used in the step-index fiber design, is currently computationally impractical.

TABLE III
GRATING PARAMETERS FOR FREE-FORM-OPTIMIZED FIBER

Grating	LP_{01}–LP_{11a}	LP_{11a}–LP_{02}	LP_{11}–LP_{21}
UV Illumination Type	Single	Single	Double
UV Illumination Angle(s) ψ	0	0	$\pi/6$ and $-\pi/6$
Modulation Depth χ	20×10^{-5}	30×10^{-5}	10×10^{-5}
Grating period Λ (μm)	1234.1	706.6	954.3
Grating length L (cm)	6.05	5.48	8.02
Chirp parameter α	4	4	4

Fig. 9 shows the transverse index profile, effective indices, and propagation constant spacings of the new design obtained with free-form index optimization. The splicing MAL and MDL STD are smaller compared to the SI design, assuming values under 0.03 dB and 0.02 dB, respectively. The propagation constant spacings $\Delta\beta_{01,11}$, $\Delta\beta_{11,02}$, and $\Delta\beta_{11,21}$ vary over wavelength by 67.1 m^{-1}, 26.7 m^{-1}, and 57.5 m^{-1}, respectively. The separation between the LP_{01}–LP_{11}, LP_{11}–LP_{02}, and LP_{11}–LP_{21} transitions and adjacent transitions is greater than 875 m^{-1}, excluding the inefficient LP_{02}–LP_{31} transition. The beat lengths of the TE_{01}/HE_{21} and TM_{01}/HE_{21} modes increase to about 0.78 m and 5.7 m, respectively.

Comparing Fig. 9(a) and Fig. 7(a) with Fig. 2(a), the free-form-optimized fiber clearly more closely resembles the transmission fiber than the SI fiber does, explaining the low splicing loss. Moreover, we are able to achieve this while further isolating the desired transitions. The greater consistency of the propagation constant spacings across all wavelengths and the longer beat lengths of LP_{11} improve the coupling efficiency as well.

Table III provides the UV illumination type and values of the modulation depth χ, grating period Λ, grating length L, and chirp α for the LP_{01}–LP_{11a}, LP_{11a}–LP_{02}, and LP_{11}–LP_{21} gratings designed using the free-form-optimized fiber. We obtain the grating parameters following the same methodology as in the step-index design case.

Fig. 10 shows the performance of the individual gratings, mode permuter, and mode permuter including splicing. Figs. 10(a) and (f) show the coupling efficiency and losses, respectively, of the LP_{01}–LP_{11a} grating. Coupling efficiency exceeds 97%, while the MAL and MDL STD are under 0.04 dB and 0.02 dB, respectively. Compared to the SI-fiber grating, there is slightly greater loss owing to the LP_{02}–LP_{31} transition being closer to the LP_{01}–LP_{11} transition. Fig. 10(k) shows the power coupling matrix at 1550nm. Compared to Fig. 8(k), we observe less unwanted mode coupling due to the increased separation between the LP_{01}–LP_{11} and LP_{11}–LP_{21} transitions.

Fig. 10(b) and (g) show the coupling efficiency and losses, respectively, for the LP_{11a}–LP_{02} grating. Coupling efficiency exceeds 98%, while the MAL and MDL STD are both under 0.02 dB. Compared to the SI-fiber grating, the losses are over 0.05 dB less at 1545 nm, validating our free-form index optimization. Fig. 10(l) shows the power coupling matrix at 1550 nm. Compared to Fig. 8(l), we observe less unwanted mode

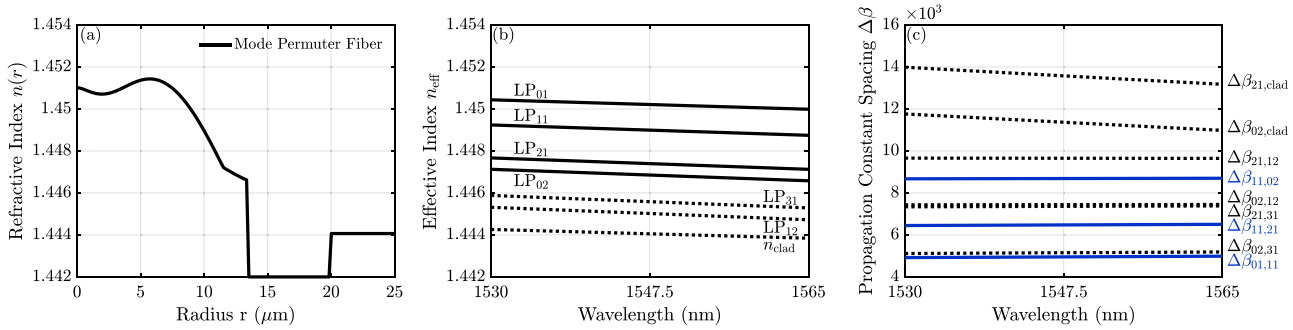

Fig. 9. Mode permuter fiber designed using free-form index optimization: (a) Transverse index profile, (b) guided mode effective indices and cladding index as a function of wavelength, and (c) select propagation constant spacings as a function of wavelength. In (b), guided modes not used for signal propagation and the cladding index are dashed. In (c), propagation constant spacings for the LP_{01}–LP_{11}, LP_{02}–LP_{12}, and LP_{11}–LP_{21} transitions are in blue, while all others are dashed.

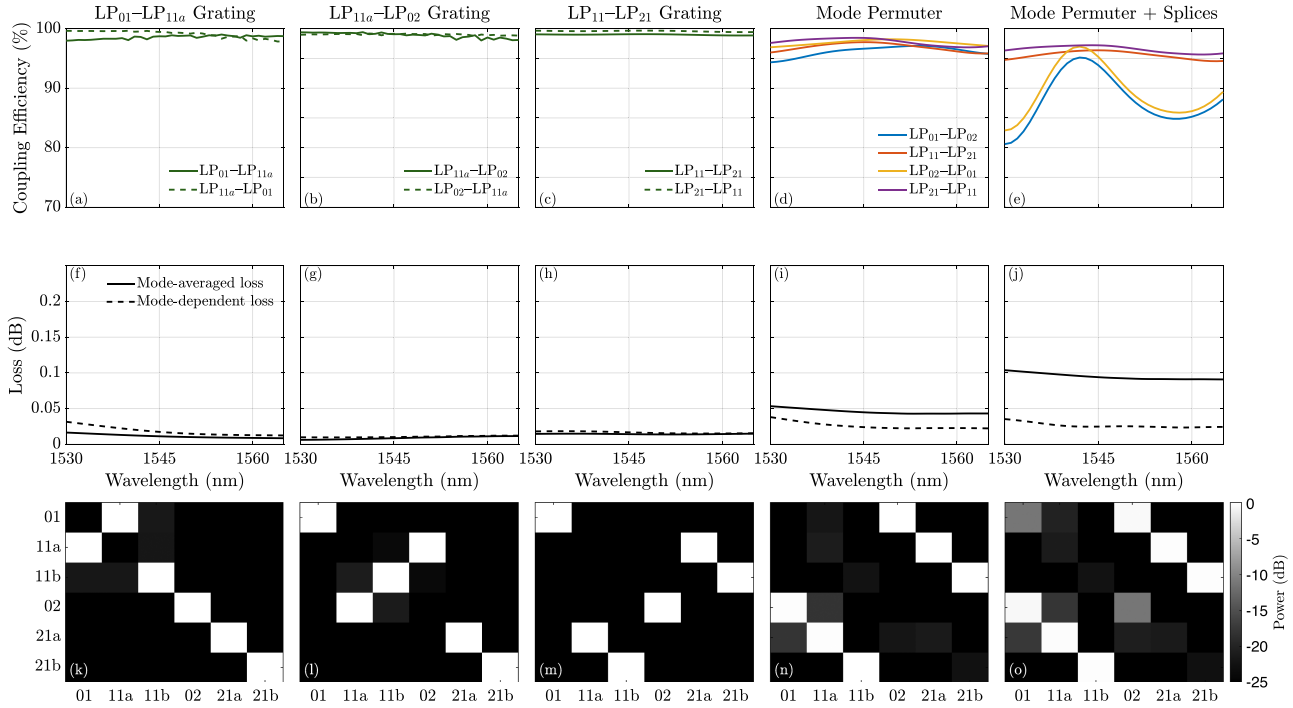

Fig. 10. Performance of individual gratings and mode permuter designed using the free-form-optimized transverse index profile in Fig. 9. Coupling efficiencies (a-e) and MAL and MDL (f-j) as a function of wavelength over the C-band of the (a, f) LP_{01}–LP_{11a} grating, (b, g) LP_{11a}–LP_{02}, (c, h) LP_{11}–LP_{21} grating, (d, i) mode permuter, and (e, j) mode permuter including splicing. Power coupling matrices (k-o) at 1550nm of the (k) LP_{01}–LP_{11a} grating, (l) LP_{11a}–LP_{02} grating, (m) LP_{11}–LP_{21} grating, (n) mode permuter, and (o) mode permuter including splicing.

coupling involving LP_{11b} due to the larger beat lengths of the TE_{01}/HE_{21} and TM_{01}/HE_{21} modes.

Fig. 10(c) and (h) show the coupling efficiencies and losses, respectively, over the C-band for the LP_{11}–LP_{21} grating. The reported coupling efficiencies are an average of those of the LP_{11a}–LP_{21a} and LP_{11b}–LP_{21b} couplings. Coupling efficiency exceeds 99%, while the MAL and MDL STD are both under 0.02 dB. Fig. 10(m) shows the power coupling matrix at 1550 nm. Like Fig. 8(m), we observe less than -25 dB of undesired mode coupling.

Fig. 10(d) and (i) show the mode permuter's coupling efficiencies and losses, respectively. The efficiencies of the LP_{01}–LP_{02}, LP_{11}–LP_{21}, LP_{02}–LP_{01}, and LP_{21}–LP_{11} couplings exceed 94%, while the MAL and MDL STD are under 0.06 dB and 0.04 dB, respectively. Fig. 10(n) shows the power coupling matrix at 1550 nm. Compared to Fig. 8(n), we observe less undesired mode coupling.

Fig. 10(e) and (j) show the mode permuter's coupling efficiencies and losses, respectively, when including splicing to and from the transmission fiber. The efficiencies of the LP_{11}–LP_{21} and LP_{21}–LP_{11} couplings exceed 95%, while those of the LP_{01}–LP_{02} and LP_{02}–LP_{01} couplings exceed 81%. The MAL rises by about 0.05 dB, whereas the MDL shows only a slight increase, similar to the SI design. Fig. 10(o) shows the power coupling matrix at 1550 nm. Compared to Fig. 8(o), we observe a significant reduction in undesired mode coupling.

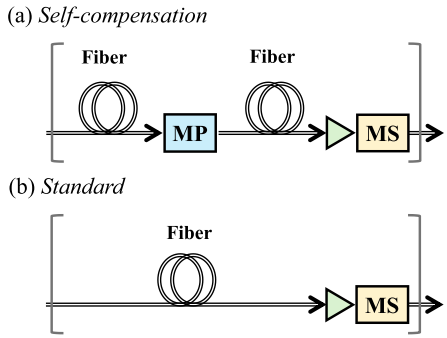

Fig. 11. Diagrams of one span of a long-haul MDM transmission link with periodic amplification and mode scrambling at the end of every span. (a) Self-compensation scheme using a mode permuter in the middle of each span. (b) Standard scheme employing only mode scramblers, serving as a baseline. MP: Mode Permuter, MS: Mode Scrambler.

A comparison of Fig. 10 with Fig. 8 demonstrates the efficacy of our index optimization strategy in enhancing performance. By leveraging the fine control over fiber propagation constants that index optimization provides, we achieve a substantial reduction in loss while increasing coupling efficiencies for all desired mode exchanges. Comparing Fig. 10(i) with Fig. 10(j) reveals that, despite the new design's reduced splicing loss, splicing to and from the mode permuter contributes more loss than the device itself. Since two splices are required for every mode permuter, this issue warrants further study.

C. Link Performance

We consider two long-haul MDM link architectures to evaluate the system performance of our mode permuter device, as shown in Fig. 11. Fig. 11(a) illustrates the self-compensation architecture, which incorporates a mode permuter in the middle of each span, as well as amplification and mode scrambling at the end of each span. Fig. 11(b) illustrates the standard architecture, which omits the mode permuter, serving as a baseline for the GD STD.

We perform numerical multisection simulations to calculate the GD STD of each link in Fig. 11. For the self-compensation architecture, we use the free-form-optimized mode permuter with characteristics given in Fig. 10. To highlight the harmful effect of splicing on GD STD reduction, we simulate the link including and excluding impairments from splicing between the mode permuter and transmission fiber. For both the self-compensation and standard architectures, the mode scrambler is assumed to equally distribute power between all modes, and the amplifier is assumed to have no MDL. We select a span length $L_S = 50$ km and assume strong random intra-group coupling in the transmission fiber [27]. We consider three random inter-group coupling lengths L_{inter} of 500 km, 2000 km, and ∞ km. $L_{\text{inter}} = \infty$ km represents a scenario with no random inter-group coupling, in which self-compensation performs the best. We normalize all GD STD values by the GD STD of one span of the standard architecture.

Fig. 12(a)–(c) show the normalized GD STD as a function of link length over $K = 100$ spans for the worst-, median-, and best-performing wavelength channels in the C-band, excluding splicing. The dashed blue line indicates the GD STD of a link employing the standard architecture in Fig. 11(b), which has GD STD proportional to the square root of the number of spans. The rise and fall of GD STD in each span clearly illustrate how effective the mode permuter is at compensating GD. The self-compensating link significantly surpasses the baseline link for all inter-group coupling lengths and wavelengths, exhibiting an end-to-end GD STD that is approximately 4 times smaller after 5000 km. Due to the stable coupling efficiency over wavelength, only minor differences in GD STD are observed between the best- and worst-performing wavelengths for $L_{\text{inter}} = \infty$ and $L_{\text{inter}} = 2000$ km. These differences nearly vanish for $L_{\text{inter}} = 500$ km because the power transfer between modes resulting from random inter-group coupling is comparable to the non-ideality of the mode permuter power transfer.

Fig. 12(d)–(f) show the normalized GD STD as a function of link length over $K = 100$ spans for the worst-, median-, and best-case wavelength channels in the C-band including splicing. While the self-compensating link continues to outperform the baseline link, the disparity between the best and worst-performing wavelengths is much more noticeable due to the effect of splicing. The best- and worst-performing wavelengths differ by a factor of 1.5 and 1.9 for random inter-group coupling lengths $L_{\text{inter}} = 500$ and $L_{\text{inter}} = \infty$ km, respectively.

Fig. 13(a) shows the normalized GD STD as a function of wavelength after $K = 100$ spans at various random inter-group coupling lengths excluding splicing. The dashed blue line indicates the link GD STD after $K = 100$ spans of the reference link, with GD STD proportional to the square root of the number of spans. The GD STD varies little over the C-band, tracking well with the stable coupling efficiencies in Fig. 10(d). We clearly see that random inter-group coupling limits GD compensation. The GD STD increases by 50% when the random inter-group coupling length decreases from $L_{\text{inter}} = \infty$ km to $L_{\text{inter}} = 500$ km.

Fig. 13(b) shows the normalized GD STD as a function of wavelength after $K = 100$ spans at various random inter-group coupling lengths including splicing. The GD STD follows the opposite trend of the LP_{01}–LP_{02} and LP_{02}–LP_{01} lines in Fig. 10(e). At 1530 nm, the GD STD is largest because the LP_{01} and LP_{02} coupling is most degraded due to splicing at this wavelength. Similarly, at 1540 nm, the GD STD is the smallest since the LP_{01} and LP_{02} coupling is least affected at this wavelength.

Figs. 12 and 13 clearly demonstrate that a well-designed mode permuter is highly effective in reducing link GD STD, decreasing GD STD by more than a factor of 3.13 across the C-band. If a mode scrambler were used in its place, the GD STD would decrease by only a factor of $\sqrt{2} \approx 1.41$ [27].

Comparing Fig. 12(a)–(c) with Fig. 12(d)–(f) shows the significant effect of unwanted coupling between LP_{01} and LP_{02} during splicing. While self-compensation offers a significant reduction in GD STD, it is crucial to minimize any unwanted coupling, particularly from splicing or from other link components.

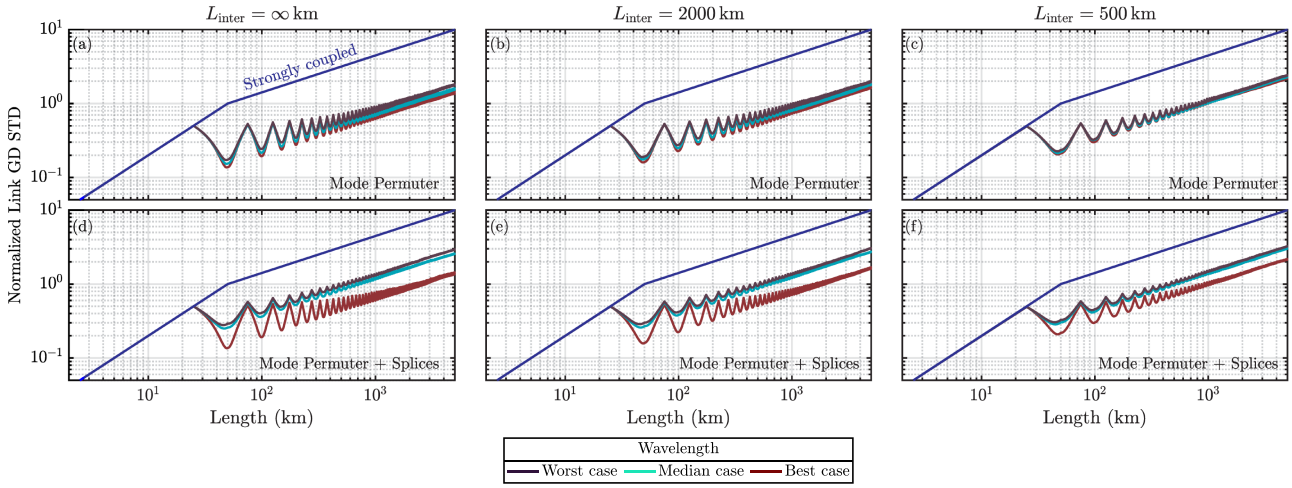

Fig. 12. Simulation of self-compensation. Normalized link GD STD as a function of length for worst-, median-, and best-performing wavelengths when (a, d) $L_{\text{inter}} = \infty$ km, (b, e) $L_{\text{inter}} = 2000$ km, and (c, f) $L_{\text{inter}} = 500$ km using the transfer matrix of the free-form-optimized mode permuter (a-c) excluding splicing and (d-f) including splicing.

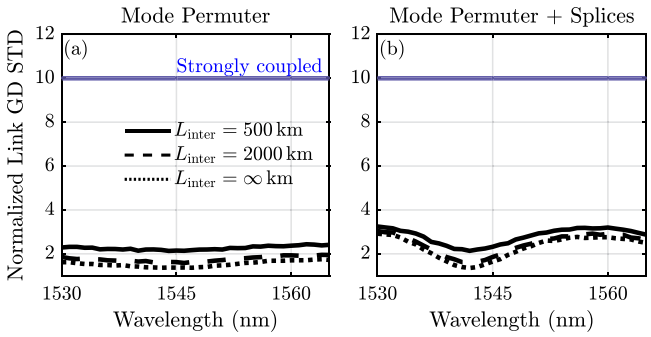

Fig. 13. Normalized link GD STD as a function of wavelength after propagation over 5000 km for L_{inter} equal to ∞, 2000, and 500km using the transfer matrix of the free-form-optimized mode permuter (a) excluding splicing and (b) including splicing.

D. Sensitivity to Fabrication Errors

In this subsection, we analyze the impact of fabrication errors on mode permuter performance.

Deviations in the transverse or longitudinal index profiles impact the power coupling between modes. These deviations can lead to insufficient coupling between desired mode pairs, unwanted coupling between other mode pairs, and increased coupling to unguided modes, resulting in reduced efficacy of self-compensation and higher losses.

We analyze how three random fabrication error scenarios affect the mode permuter losses and the GD STD of a $K = 100$-span link employing a self-compensation architecture, as shown in Fig. 11(a). The three fabrication error scenarios are:

1) *Random transverse index profile errors:* Each mode permuter's index profile $n(r)$ is subject to an independent realization of an error $\delta n(r)$ computed from

$$\delta n(r) = \sum_{i=1}^{N} A_i \cos(2\pi f_i r + \phi_i) + B_i \sin(2\pi f_i r + \theta_i), \tag{21}$$

where N is the number of sinusoids used in the expansion of the random deviation, f_i are the spatial frequencies, A_i and B_i are the amplitudes of the spatial frequencies, and ϕ_i and θ_i are random phase offsets [11], [55]. Random deviations are produced with $N = 5$ and f_i linearly spaced from 5×10^4 m^{-1} to 20×10^4 m^{-1}. ϕ_i and θ_i are uniformly distributed from 0 to 2π radians and A_i and B_i are sampled from a zero-mean Gaussian distribution with unit variance, $A_i, B_i \sim \mathcal{N}(0, 1)$. A_i and B_i are then scaled so that $\delta n(r)$ has a desired RI error STD [11], [55].

2) *Random grating period errors:* The grating period Λ of each mode permuter is subject to an independent realization of an error $\delta\Lambda \sim \mathcal{N}(0, \sigma_\Lambda^2)$, where σ_Λ is the grating period error STD.

3) *Random modulation depth errors:* The modulation depth χ of each mode permuter is subject to an independent realization of an error $\delta\chi \sim \mathcal{N}(0, \sigma_\chi^2)$, where σ_χ is the modulation depth error STD.

We perform this study only on the mode permuter using a free-form optimized fiber, described in Section IV-B. We expect the results to be similar for the mode permuter using a SI fiber. In the evaluation of the GD STD, we assume that the inter-group coupling length is $L_{\text{inter}} = \infty$ km. The following results are all at 1550 nm.

Fig. 14(a)–(c) shows the average mode permuter MDL STD and MAL as a function of the RI error STD, grating period error STD σ_Λ, and modulation depth error STD σ_χ, respectively. The mode permuter MAL and MDL STD increase with increasing RI error STD. However, even with an RI error STD of 10×10^{-5}, the MAL and MDL STD increase by less than 0.05dB. Similarly, variations in grating period and modulation depth within the studied ranges result in only minor increases in loss. This robustness can be attributed to the intentional design of the transverse index profile with well-separated mode transitions. Significant loss would be expected only under severe perturbations that allow signal modes to phase-match with unintended guided or radiation modes.

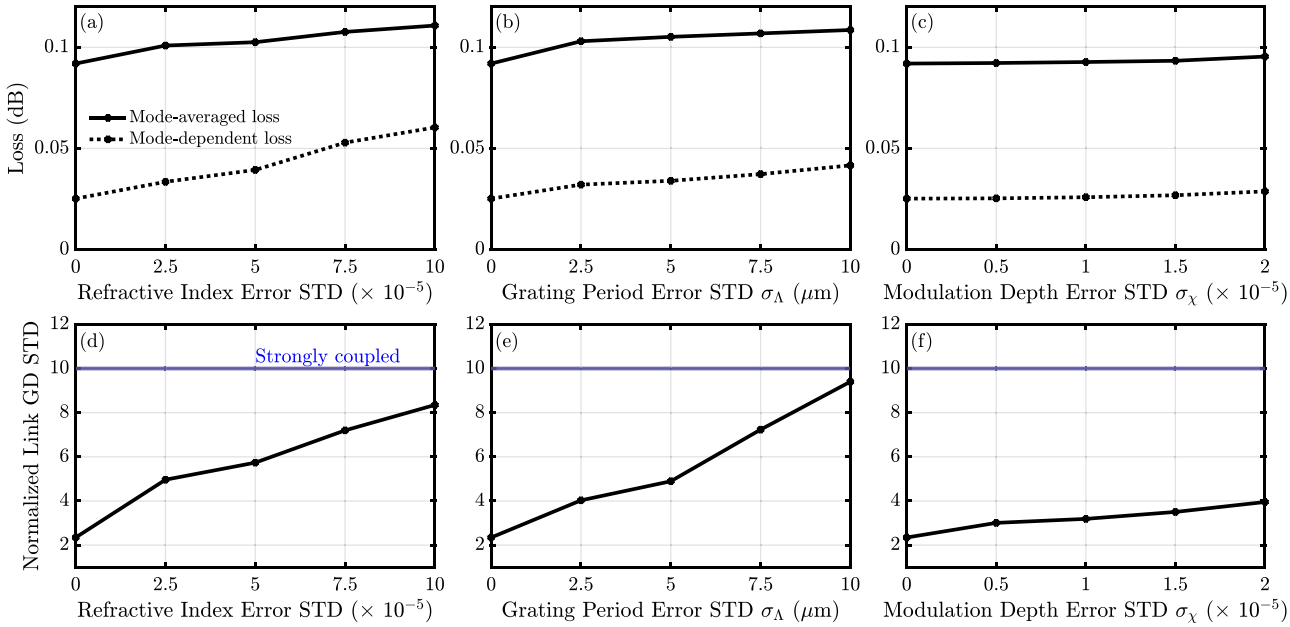

Fig. 14. Impact of random fabrication errors on the mode permuter loss (a-c) and the GD STD of a $K = 100$-span link employing a self-compensation architecture (d-f). (a) Average mode permuter MAL and MDL as a function of RI error STD. (b) Average mode permuter MAL and MDL as a function of grating period error STD σ_Λ. (c) Average mode permuter MAL and MDL as a function of modulation depth error STD σ_χ. (d) Average normalized GD STD as a function of RI error STD. (e) Average normalized GD STD as a function of grating period error STD σ_Λ. (f) Average normalized GD STD as a function of modulation depth error STD σ_χ.

Fig. 14(d) shows the average normalized GD STD as a function of the RI error STD. At the maximum tested value of 10×10^{-5}, the average normalized GD STD increases by a factor of 4, indicating that self-compensation has been almost entirely disrupted. To keep the average normalized GD STD below 5, the refractive index error must be limited to approximately 3×10^{-5}. This highlights the importance of precise control in fiber fabrication to preserve the self-compensating behavior of the mode permuter.

Fig. 14(e) shows the average normalized GD STD as a function of the grating period error STD σ_Λ. Similarly, at the largest grating error STD of 10 μm, self-compensation is entirely suppressed with the average normalized GD STD nearly reaching 10. A σ_Λ of approximately 5 μm is needed to keep the average normalized GD STD below 5. This tolerance is achievable with current fabrication methods, as fiber gratings with sub-micron periods are commercially available.

Fig. 14(f) shows the average normalized GD STD as a function of the modulation depth error STD σ_χ. The average normalized GD STD is below 5 for all studied modulation depth error STDs, indicating that the mode permuter is relatively insensitive to modulation depth variations. This is expected, as small changes in modulation depth do not significantly affect phase matching.

Fig. 14 shows that maintaining tight fabrication tolerances allows the mode permuter to be most effective in reducing GD STD. From the coupling efficiency relation in (13), increasing the modulation depth, and thus the coupling coefficient κ, can reduce the sensitivity of the coupling efficiency to phase mismatch. However, this must be balanced against the risk of introducing additional unwanted mode coupling, which will increase loss.

V. Discussion

A. Manufacturing Methods

While the step-index mode permuter design is readily realizable with standard fiber and grating manufacturing techniques [34], [35], [57], [58], fabricating the mode permuter with a free-form transverse index profile is an important challenge. GI fibers, which bear resemblance to the free-form index profile, can be precisely manufactured using plasma-enhanced chemical vapor deposition [54], [59], [60], [61] and can have gratings induced through ultraviolet laser exposure [62], CO_2 laser irradiation [63], or mechanical pressure plates [40]. However, obtaining the transverse index profile as described here may still be challenging with plasma-enhanced chemical vapor deposition. Recent advances in fabricating fused silica optical fibers with nanostructured cores demonstrate great potential in overcoming existing challenges in creating arbitrary transverse index profile fibers, as demonstrated by the fabrication of GI fiber [64] and square-like core fiber [65]. Notably, this technique has been reported to enable the realization of arbitrary transverse index profiles [66]. Furthermore, gratings have been successfully inscribed in nanostructured core fibers using ultraviolet laser exposure [67], [68], [69].

A further critical challenge lies in precise grating inscription. To maintain consistent illumination angles across all gratings, the fiber must be kept straight between rotatable fiber clamps, as demonstrated in [35]. For double-sided illumination, the fiber can be rotated from both ends to the necessary orientation [35]. After fabrication, the mode permuter can be mounted in a dedicated fixture that prevents twisting and subsequently spliced into the transmission link. Minimizing twist is critical, since the

LP_{01}–LP_{02} conversion implemented with three gratings relies on maintaining a consistent grating orientation.

Numerical simulations evaluating the bend sensitivity of the proposed design indicate that coupling performance degrades significantly for bending radii below approximately 200 mm. Thus, the mode permuter cannot be wound on a narrow spool. Since the longest device is only about 25 cm, we do not believe this restriction would severely impact feasibility.

B. Splicing

As noted in Section IV, undesired coupling between the LP_{01} and LP_{02} modes and loss due to splicing remain the primary performance impairments even for the free-form-optimized design. These issues can potentially be ameliorated by optimizing the fusion splicing process or using intermediate bridge fibers. Reference [70] shows how varying the arc length duration during fusion splicing reduces crosstalk between LP_{01} and LP_{02} from -15 dB to -25 dB for an SMF to MMF splice. This would significantly minimize the wavelength variation of the link GD STD. Hence, optimizing the splicing process may be crucial for self-compensation and warrants further study.

C. Extending to More Mode Groups

The principles used to determine an ideal mode permutation scheme can be extended to any number of mode groups N_g using the theoretical framework described in Section II. [45] describes a general approach for arbitrary N_g. While such mode permutation schemes exist, their implementation becomes more difficult as N_g increases and more challenges arise.

To illustrate these challenges, we study the case of $N_g = 4$ mode groups and $D = 20$ guided spatial and polarization modes, corresponding to the LP_{01}, LP_{11a}, LP_{11b}, LP_{02}, LP_{21a}, LP_{21b}, LP_{12a}, LP_{12b}, LP_{31a}, and LP_{31b} spatial modes in two polarizations. As described in [45], we can find an optimal self-compensation scheme by partitioning the mode groups into two groups, each with a different mode-group-averaged GD from the set $\{-\tau, \tau\}$. In this scheme, the ideal mode-group-averaged GD vector is $\boldsymbol{\tau}_0 = [\tau, -\tau, -\tau, \tau]^T$. By minimizing (4) subject to the constraints in (5), we can find an optimal $\boldsymbol{\mathcal{P}}_{\text{MP}}$ given by

$$\boldsymbol{\mathcal{P}}_{\text{MP}} = \begin{bmatrix} 0 & 1 & 0 & 0 \\ 1 & 0 & 0 & 1 \\ 0 & 0 & 0 & 3 \\ 0 & 1 & 3 & 0 \end{bmatrix}. \tag{22}$$

It can be verified that this scheme results in ideal self-compensation in the absence of any impairments.

Some of the mode exchanges in $\boldsymbol{\mathcal{P}}_{\text{MP}}$ occur between mode groups with vastly different propagation constants (in particular, between the second and fourth mode groups). These cannot be coupled directly without also causing coupling into the cladding and subsequent loss. Thus, such distant mode exchanges must be performed stepwise, sequentially exchanging power between adjacent mode groups until the final destination is reached. This significantly increases the number of gratings required. For the particular mode permutation scheme described in [45], the minimum number of required gratings follows:

$$G(N_g) = \left\lfloor \frac{N_g}{4} \right\rfloor \left(2N_g + \left\lceil \frac{N_g - 1}{2} \right\rceil - 4 \left\lfloor \frac{N_g}{4} \right\rfloor \right) \tag{23}$$

A derivation is given in Appendix A. For this example, $G(4) = 6$.

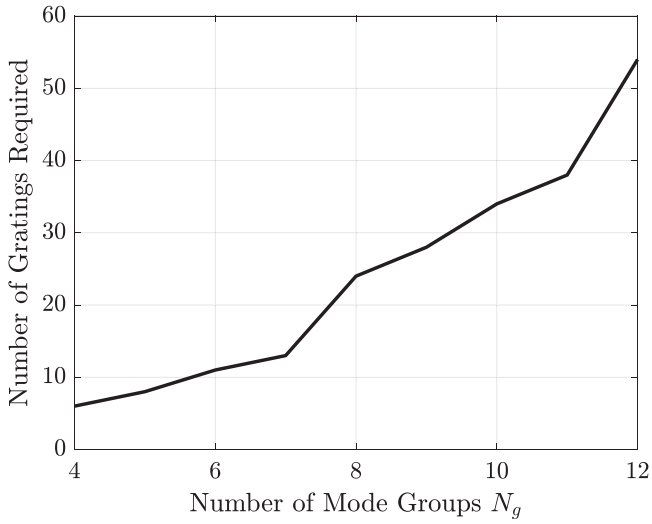

Fig. 15. Minimum number of gratings required for optimal self-compensation as a function of the number of mode groups N_g for the permutation scheme described in [45].

Fig. 15 shows the minimum number of gratings required for optimal self-compensation as a function of the number of mode groups N_g. The curve follows the approximation $G(N_g) \approx 3N_g^2/8$, which is exact when N_g is a multiple of 4. Due to the floor functions in the exact expression, the number of gratings increases sharply at multiples of 4.

The design space of each of these gratings becomes more constrained as the number of modes rises. With more modes, there are more potential paths for undesired coupling. Every propagation constant spacing for an undesired transition must be separated from the desired transitions, and both types become more numerous as N_g rises, further limiting potential grating options. At some point, separating all of these spacings within a single fiber may become intractable, necessitating multiple mode permutation fibers spliced together. This will impact the splicing loss.

The mode permuter device must be designed jointly with the transmission fiber to ensure the group delay vector aligns with the permutation scheme and that the fibers' mode fields maximally overlap to limit splicing loss. Transmission fiber design has its own unique design challenges when N_g is large [45]. These are topics for further study.

D. Alternative Types of Mode Permuters

Mode permuters can also be realized using multi-plane light converters (MPLCs) [15], [18], [22], [71] or mode-selective photonic lanterns (MSPLs) [28], [72], [73]. These approaches are appealing because they can implement arbitrary mode permutations without requiring the specialized fiber and grating designs

of LPFG-based mode permuters. However, MPLCs and MSPLs typically exhibit substantially higher MALs and MDLs on the order of 1 dB [28], [71], [73], [74]. In long-haul systems where hundreds of mode permuters must be cascaded, these losses accumulate to impractical levels. Consequently, despite their flexibility, MPLCs and MSPLs still require more development before practical deployment as mode permuters in long-haul links becomes feasible.

VI. Conclusion

We described a self-compensation scheme for an MDM link supporting $D = 12$ spatial and polarization modes. This scheme relied on the modes in the first two mode groups having equal and opposite modal dispersions compared to those of the third mode group, along with a mode permuter that exchanges all power between the third mode group and the first two mode groups. We proposed a mode permuter design with a cascade of four LPFGs exchanging the following pairs of modes: LP_{01}–LP_{11a}, LP_{11a}–LP_{02}, LP_{01}–LP_{11a}, and LP_{11}–LP_{21}. Then, we described a strategy for designing the mode permuter fiber transverse index profile and the grating index profiles.

We first designed a mode permuter with gratings inscribed on SI fiber, using grid search to find an SI fiber with low splicing loss to the transmission fiber and well-separated propagation constant spacings for the LP_{01}–LP_{11}, LP_{11}–LP_{02}, and LP_{11}–LP_{02} transitions. Then, chirped gratings were designed for each mode exchange to have low MAL and MDL, while maintaining high transmission over the C-band. This resulted in a mode permuter design with transmission over 75% for all desired mode power exchanges, a MAL of less than 0.25 dB, and an MDL of less than 0.11 dB over the C-band. From analyzing this design, we found that splicing loss, undesired coupling between LP_{01} and LP_{02} from splicing, and LP_{11a}–LP_{02} grating loss are key performance limiters.

To address these issues, we designed an improved transverse index profile using free-form index optimization. This yielded a mode permuter design with transmission over 81% for all desired mode exchanges, a MAL of less than 0.11 dB, and an MDL of less than 0.04 dB over the C-band.

We numerically evaluated the designs through link simulations and investigated the reduction in GD spread for different levels of random inter-group coupling in the fiber. Our results showed that periodic mode permutation and mode scrambling reduces a link's GD STD by a factor exceeding 3.13 compared to a link relying solely on periodic mode scrambling.

Finally, we performed numerical simulations to study how transverse and longitudinal index profile fabrication errors affect the mode permuter MAL and MDL STD and link GD STD.

Appendix
Deriving the LPFG Scaling Law for Extending to More Mode Groups

To determine the minimum required number of gratings for the mode permutation scheme discussed in [45], we start with the example of $N_g = 4$ mode groups described in Section V-C. The optimal $\boldsymbol{\mathcal{P}}_{\text{MP}}$ is given by

$$\boldsymbol{\mathcal{P}}_{\text{MP}} = \begin{bmatrix} 0 & 1 & 0 & 0 \\ 1 & 0 & 0 & 1 \\ 0 & 0 & 0 & 3 \\ 0 & 1 & 3 & 0 \end{bmatrix}. \tag{24}$$

We can see there are three distinct sets of gratings required to achieve this permutation:

1) One grating is needed to exchange one mode between mode groups 1 and 2.
2) $(N_g - 2) + (N_g - 3) = 2N_g - 5 = 3$ gratings are needed to exchange one mode between the second and final mode groups. Coupling these modes directly with a single grating would cause undesired coupling into the cladding and subsequent loss, so we perform this exchange stepwise, only coupling modes in adjacent mode groups until the final permutation is ultimately achieved.
3) $\left\lceil \frac{N_g - 1}{2} \right\rceil = 2$ gratings for $N_g - 1 = 3$ mode exchanges between the final and penultimate mode groups. In this category of gratings, most exchange two pairs of modes, since a, b pairs of the same LP mode can be exchanged with the same grating. If $N_g - 1$ is odd, then an additional grating performs the remaining mode exchange.

For $N_g = 4$, we can sum over each of these three sets of gratings for a total of $1 + 2N_g - 5 + \left\lceil \frac{N_g - 1}{2} \right\rceil = 1 + 3 + 2 = 6$ required gratings at minimum. As we extend to more mode groups, each additional set of four mode groups requires an additional three sets of gratings. For each additional mode exchange added to category (1), one is removed from category (3), so the total number of gratings required for both categories combined remains constant at $1 + \left\lceil \frac{N_g - 1}{2} \right\rceil$ for each set of four mode groups. For the set of four mode groups comprised of the first two and last two mode groups, the number of gratings required in category (2) is the highest, at $2N_g - 5$. For each subsequent set of four mode groups, moving inwards towards those of intermediate order, the number of required gratings in category (2) decreases by 8. To determine the total number of gratings, we can sum each of these three categories over all $\left\lfloor \frac{N_g}{4} \right\rfloor$ sets of 4 mode groups, yielding:

$$\begin{aligned} G(N_g) &= \sum_{i=1}^{\lfloor N_g/4 \rfloor} 1 + [2N_g - 5 - 8(i-1)] + \left\lceil \frac{N_g - 1}{2} \right\rceil \\ &= \sum_{i=1}^{\lfloor N_g/4 \rfloor} 2N_g - 4 + \left\lceil \frac{N_g - 1}{2} \right\rceil - 8 \sum_{i=0}^{\lfloor N_g/4 \rfloor - 1} i \\ &= \left(2N_g - 4 + \left\lceil \frac{N_g - 1}{2} \right\rceil\right) \left\lfloor \frac{N_g}{4} \right\rfloor - 8 \left\lfloor \frac{N_g}{4} \right\rfloor \left(\left\lfloor \frac{N_g}{4} \right\rfloor - 1 \right) / 2 \\ &= \left\lfloor \frac{N_g}{4} \right\rfloor \left(2N_g + \left\lceil \frac{N_g - 1}{2} \right\rceil - 4 \left\lfloor \frac{N_g}{4} \right\rfloor \right) \end{aligned} \tag{25}$$

For the case where N_g is a multiple of 4, this reduces to:

$$G(N_g) = 3N_g^2/8 \tag{26}$$

ACKNOWLEDGMENT

The authors would like to thank the Stanford Research Computing Center for providing this cluster and technical support. Much of the computing for this project was performed on the Sherlock cluster at Stanford University.

REFERENCES

[1] H. Srinivas et al., "Modeling and experimental measurement of power efficiency for power-limited SDM submarine transmission systems," *J. Lightw. Technol.*, vol. 39, no. 8, pp. 2376–2386, Apr. 2021. [Online]. Available: https://ieeexplore.ieee.org/document/9314868

[2] O. V. Sinkin, A. V. Turukhin, W. W. Patterson, M. A. Bolshtyansky, D. G. Foursa, and A. N. Pilipetskii, "Maximum optical power efficiency in SDM-Based optical communication systems," *IEEE Photon. Technol. Lett.*, vol. 29, no. 13, pp. 1075–1077, Jul. 2017. [Online]. Available: https://ieeexplore.ieee.org/document/7919195

[3] O. V. Sinkin et al., "SDM for power-efficient undersea transmission," *J. Lightw. Technol.*, vol. 36, no. 2, pp. 361–371, Jan. 2018.

[4] J.-X. Cai et al., "9 Tb/s transmission using 29 mW optical pump power per EDFA with 1.24 tb/s/w optical power efficiency over 15,050 km," *J. Lightw. Technol.*, vol. 40, no. 6, pp. 1650–1657, Mar. 2022. [Online]. Available: https://ieeexplore.ieee.org/document/9626578

[5] W. Klaus et al., "Advanced space division multiplexing technologies for optical networks [Invited]," *J. Opt. Commun. Netw.*, vol. 9, no. 4, pp. C1–C11, Apr. 2017. [Online]. Available: https://ieeexplore.ieee.org/document/7901441

[6] P. J. Winzer, R. Ryf, and S. Randel, "Chapter 10 - spatial multiplexing using multiple-input multiple-output signal processing," in *Optical Fiber Telecommunications (Sixth Edition)* (Optics and Photonics Series), I. P. Kaminow, T. Li, and A. E. Willner, Eds. Boston: Academic Press, Jan. 2013, pp. 433–490. [Online]. Available: https://www.sciencedirect.com/science/article/pii/B9780123969606000109

[7] H. Srinivas, O. Krutko, and J. M. Kahn, "Efficient integrated multimode amplifiers for scalable long-haul SDM transmission," *J. Lightw. Technol.*, vol. 41, no. 15, pp. 4989–5002, Aug. 2023. [Online]. Available: https://ieeexplore.ieee.org/document/10064021

[8] R. V. Jensen, L. Grüner-Nielsen, N. H. L. Wong, Y. Sun, Y. Jung, and D. J. Richardson, "Demonstration of a 9 LP-Mode transmission fiber with low DMD and loss," presented at the Opt. Fiber Commun. Conf., Los Angeles, CA, USA, Mar. 22–26, 2015, Paper W2A.34. [Online]. Available: https://opg.optica.org/abstract.cfm?uri=OFC-2015-W2A.34

[9] R. Ryf et al., "Mode-multiplexed transmission over conventional graded-index multimode fibers," *Opt. Exp.*, vol. 23, no. 1, pp. 235–246, Jan. 2015. [Online]. Available: https://opg.optica.org/oe/abstract.cfm?uri=oe-23-1-235

[10] N. K. Fontaine et al., "Characterization of space-division multiplexing systems using a swept-wavelength interferometer," in *Proc. 2013 Opt. Fiber Commun. Conf. Expo. Nat. Fiber Opt. Engineers Conf.*, Mar. 2013, pp. 1–3. [Online]. Available: https://ieeexplore.ieee.org/abstract/document/6533121

[11] O. Krutko, R. Refaee, A. Vijay, and J. M. Kahn, "Ultra-low-Loss fiber Bragg grating mode scrambler design exploiting propagation constant engineering," *J. Lightw. Technol.*, vol. 43, no. 6, pp. 2883–2896, Mar. 2025. [Online]. Available: https://opg.optica.org/jlt/abstract.cfm?uri=jlt-43-6-2883

[12] K.-P. Ho and J. M. Kahn, "Mode-dependent loss and gain: Statistics and effect on mode-division multiplexing," *Opt. Exp.*, vol. 19, no. 17, pp. 16612–16635, Aug. 2011. [Online]. Available: https://opg.optica.org/oe/abstract.cfm?uri=oe-19-17-16612

[13] K.-P. Ho and J. M. Kahn, "Frequency diversity in mode-division multiplexing systems," *J. Lightw. Technol.*, vol. 29, no. 24, pp. 3719–3726, Dec. 2011. [Online]. Available: https://ieeexplore.ieee.org/document/6060841

[14] G. Rademacher, S. Warm, and K. Petermann, "Nonlinear interaction in differential mode delay managed mode-division multiplexed transmission systems," *Opt. Exp.*, vol. 23, no. 1, pp. 55–60, Jan. 2015. [Online]. Available: https://opg.optica.org/oe/abstract.cfm?URI=oe-23-1-55

[15] Y. Wakayama, D. Soma, K. Igarashi, H. Taga, and T. Tsuritani, "Intermediate mode interchange for reduction of differential mode-group delay in weakly-coupled 6-Mode fiber transmission line," presented at the *Opt. Fiber Commun. Conf.*, Anaheim, CA, USA, Mar. 20–26, 2016, Paper M3E.6. [Online]. Available: https://opg.optica.org/abstract.cfm?uri=OFC-2016-M3E.6

[16] G. Di Sciullo et al., "Modal dispersion mitigation in a long-haul 15-Mode fiber link through mode permutation," in *Proc. IEEE Photon. Soc. Summer Topicals Meeting Ser.*, Jul. 2023, pp. 1–2, [Online]. Available: https://ieeexplore.ieee.org/document/10224367

[17] H. Wang et al., "New mode-group-permutation strategies for MDL reduction in long-haul MDM systems," presented at the *Opt. Fiber Commun. Conf.*, San Diego CA, USA, Mar. 5–9, 2013, Paper W3E.7. [Online]. Available: https://opg.optica.org/abstract.cfm?uri=OFC-2023-W3E.7

[18] Y. Wang et al., "Novel mirror-flipped mode permutation technique for long-haul mode-division multiplexing transmissions," presented at the *Opt. Fiber Commun. Conf.*, San Diego, CA, USA, Mar. 6–10, 2022, Paper M4B.5. [Online]. Available: https://opg.optica.org/abstract.cfm?uri=OFC-2022-M4B.5

[19] T. Xu et al., "Modal gain equalization of few-mode erbium-doped fiber amplifiers enabled by mirrored mode exchanges," presented at the *Opt. Fiber Commun. Conf.*, San Diego CA, USA, Mar. 5–9, 2023, Paper M1B.3. [Online]. Available: https://opg.optica.org/abstract.cfm?uri=OFC-2023-M1B.3

[20] H. Fan et al., "Compact cyclic fiber three-mode converter based on mechanical fiber grating," *Opt. Lett.*, vol. 47, no. 17, pp. 4419–4422, Sep. 2022. [Online]. Available: https://opg.optica.org/ol/abstract.cfm?uri=ol-47-17-4419

[21] K. Shibahara, T. Mizuno, H. Ono, K. Nakajima, and Y. Miyamoto, "Long-haul DMD-Unmanaged 6-Mode-Multiplexed transmission employing cyclic mode-group permutation," presented at the *Opt. Fiber Commun. Conf.*, San Diego, CA, USA, Mar. 8–12, 2020, Paper Th3H.3. [Online]. Available: https://opg.optica.org/abstract.cfm?uri=OFC-2020-Th3H.3

[22] G. Di Sciullo et al., "Enhancing long-haul 15-Mode fiber performance: Mode permutation for reduced modal dispersion," *J. Lightw. Technol.*, vol. 43, no. 2, pp. 481–491, Jan. 2025. [Online]. Available: https://ieeexplore.ieee.org/document/10663941

[23] K. Shibahara, M. Hoshi, and Y. Miyamoto, "10-Spatial-Mode 1300-Km transmission over 6-LP graded index few-mode fiber with 36-Ns modal dispersion," *J. Lightw. Technol.*, vol. 42, no. 4, pp. 1257–1264, Feb. 2024. [Online]. Available: https://ieeexplore.ieee.org/document/10294195/

[24] K.-P. Ho and J. M. Kahn, "Mode coupling and its impact on spatially multiplexed systems," in *Proc. Opt. Fiber Telecommun.* 2013, pp. 491–568. [Online]. Available: https://linkinghub.elsevier.com/retrieve/pii/B9780123969606000110

[25] K.-P. Ho and J. M. Kahn, "Statistics of group delays in multimode fiber with strong mode coupling," *J. Lightw. Technol.*, vol. 29, no. 21, pp. 3119–3128, Nov. 2011.

[26] K.-P. Ho and J. M. Kahn, "Linear propagation effects in mode-division multiplexing systems," *J. Lightw. Technol.*, vol. 32, no. 4, pp. 614–628, Feb. 2014. [Online]. Available: https://ieeexplore.ieee.org/document/6615972

[27] A. Vijay, O. Krutko, R. Refaee, and J. M. Kahn, "Modal statistics in mode-division-multiplexed systems using mode scramblers," *J. Lightw. Technol.*, vol. 43, no. 2, pp. 845–856, Jan. 2025. [Online]. Available: https://ieeexplore.ieee.org/document/10685071/?arnumber=10685071

[28] S. O. Arık, K.-P. Ho, and J. M. Kahn, "Group delay management and multiinput multioutput signal processing in mode-division multiplexing systems," *J. Lightw. Technol.*, vol. 34, no. 11, pp. 2867–2880, Jun. 2016. [Online]. Available: https://ieeexplore.ieee.org/document/7409913

[29] W. Jin and K. S. Chiang, "Mode converters based on cascaded long-period waveguide gratings," *Opt. Lett.*, vol. 41, no. 13, pp. 3130–3133, Jul. 2016. [Online]. Available: https://opg.optica.org/ol/abstract.cfm?uri=ol-41-13-3130

[30] Y. Wang, "Review of long period fiber gratings written by CO_2 laser," *J. Appl. Phys.*, vol. 108, no. 8, Oct. 2010, Art. no. 081101. [Online]. Available: https://aip.scitation.org/doi/10.1063/1.3493111

[31] D. Askarov and J. M. Kahn, "Long-period fiber gratings for mode coupling in mode-division-multiplexing systems," *J. Lightw. Technol.*, vol. 33, no. 19, pp. 4032–4038, Oct. 2015.

[32] Y. Zhao, H. Chen, N. K. Fontaine, J. Li, R. Ryf, and Y. Liu, "Broadband and low-loss mode scramblers using CO_2-laser inscribed long-period gratings," *Opt. Lett.*, vol. 43, no. 12, pp. 2868–2871, Jun. 2018. [Online]. Available: https://opg.optica.org/ol/abstract.cfm?uri=ol-43-12-2868

[33] Y. Ma, C. Jiang, Z. Liu, C. Mou, and Y. Liu, "High-order OAM mode generator using multi-cascaded long-period fiber gratings," *IEEE Photon. Technol. Lett.*, vol. 35, no. 8, pp. 434–437, Apr. 2023. [Online]. Available: https://ieeexplore.ieee.org/document/10064136/?arnumber=10064136

[34] X. Wang, H. Guo, Z. Shi, W. Chang, Z. Wang, and Y.-G. Liu, "Efficient mutual conversion of high-order core mode in few-mode fiber employing long period fiber gratings," *J. Lightw. Technol.*, vol. 42, no. 7, pp. 2464–2472, Apr. 2024. [Online]. Available: https://ieeexplore.ieee.org/document/10342848/?arnumber=10342848

[35] X. Wang, H. Guo, Z. Shi, W. Chang, Z. Wang, and Y.-G. Liu, "Broadband conversion between high-order angular modes based on double-sided exposure long-period fiber grating," *Opt. Exp.*, vol. 32, no. 22, Art. no. 40060, Oct. 2024. [Online]. Available: https://opg.optica.org/abstract.cfm?URI=oe-32-22-40060

[36] Y. Zhao, Y. Liu, L. Zhang, C. Zhang, J. Wen, and T. Wang, "Mode converter based on the long-period fiber gratings written in the two-mode fiber," *Opt. Exp.*, vol. 24, no. 6, pp. 6186–6195, Mar. 2016. [Online]. Available: https://opg.optica.org/oe/abstract.cfm?uri=oe-24-6-6186

[37] X. Zhao et al., "Mode converter based on the long-period fiber gratings written in the six-mode fiber," in *Proc. 16th Int. Conf. Opt. Commun. Netw.*, Aug. 2017, pp. 1–3. [Online]. Available: https://ieeexplore.ieee.org/document/8121432/?arnumber=8121432

[38] Y. Zhao, Z. Liu, Y. Liu, C. Mou, T. Wang, and Y. Yang, "Ultra-broadband fiber mode converter based on apodized phase-shifted long-period gratings," *Opt. Lett.*, vol. 44, no. 24, pp. 5905–5908, Dec. 2019. [Online]. Available: https://opg.optica.org/ol/abstract.cfm?uri=ol-44-24-5905

[39] K. Shibahara et al., "DMD-Unmanaged long-haul SDM transmission over 2500-km 12-core -mode MC-FMF and 6300-km 3-mode FMF employing intermodal interference cancelling technique," in *Proc. 2018 Opt. Fiber Commun. Conf. Expo.*, Mar. 2018, pp. 1–3. [Online]. Available: https://ieeexplore.ieee.org/document/8386375/?arnumber=8386375

[40] H. Liu et al., "Reducing group delay spread using uniform long-period gratings," *Sci. Rep.*, vol. 8, no. 1, Mar. 2018, Art. no. 3882. [Online]. Available: https://www.nature.com/articles/s41598-018-21609-1

[41] C. Antonelli, A. Mecozzi, M. Shtaif, and P. J. Winzer, "Stokes-space analysis of modal dispersion in fibers with multiple mode transmission," *Opt. Exp.*, vol. 20, no. 11, pp. 11718–11733, May 2012. [Online]. Available: https://opg.optica.org/oe/abstract.cfm?uri=oe-20-11-11718

[42] C. Antonelli and A. Mecozzi, "Near-zero modal-dispersion (NEMO) coupled-core multi-core fibers," *J. Lightw. Technol.*, vol. 39, no. 23, pp. 7517–7528, Dec. 2021. [Online]. Available: https://opg.optica.org/jlt/abstract.cfm?uri=jlt-39-23-7517

[43] C. Antonelli, A. Mecozzi, M. Shtaif, N. K. Fontaine, H. Chen, and R. Ryf, "Stokes-space analysis of modal dispersion of SDM fibers with mode-dependent loss: Theory and experiments," *J. Lightw. Technol.*, vol. 38, no. 7, pp. 1668–1677, Apr. 2020. [Online]. Available: https://ieeexplore.ieee.org/document/8932545

[44] S. O. Arık, K.-P. Ho, and J. M. Kahn, "Delay spread reduction in mode-division multiplexing: Mode coupling versus delay compensation," *J. Lightw. Technol.*, vol. 33, no. 21, pp. 4504–4512, Nov. 2015.

[45] A. Vijay, N. Zahedi, O. Krutko, R. Refaee, and J. M. Kahn, "Closed-form statistics and design of mode-division-multiplexing systems employing group-delay compensation and mode permutation," *J. Lightw. Technol.*, vol. 43, pp. 10828–10840, May 2025.

[46] S. Fan and J. M. Kahn, "Principal modes in multimode waveguides," *Opt. Lett.*, vol. 30, no. 2, pp. 135–137, Jan. 2005. [Online]. Available: https://opg.optica.org/ol/abstract.cfm?uri=ol-30-2-135

[47] J. Carpenter, B. J. Eggleton, and J. Schröder, "Observation of Eisenbud–Wigner–Smith states as principal modes in multimode fibre," *Nature Photon.*, vol. 9, no. 11, pp. 751–757, Nov. 2015. [Online]. Available: https://www.nature.com/articles/nphoton.2015.188

[48] T. Mori, T. Sakamoto, M. Wada, T. Yamamoto, and F. Yamamoto, "Low DMD four LP mode transmission fiber for wide-band WDM-MIMO system," in *Proc. Opt. Fiber Commun. Conf. Expo. Nat. Fiber Opt. Engineers Conf.*, Mar. 2013, pp. 1–3. [Online]. Available: https://ieeexplore.ieee.org/document/6532923

[49] H. Kogelnik and P. J. Winzer, "Modal birefringence in weakly guiding fibers," *J. Lightw. Technol.*, vol. 30, no. 14, pp. 2240–2245, Jul. 2012. [Online]. Available: https://ieeexplore.ieee.org/abstract/document/6193400

[50] J. Fang, A. Li, and W. Shieh, "Low-DMD few-mode fiber with distributed long-period grating," *Opt. Lett.*, vol. 40, no. 17, pp. 3937–3940, Sep. 2015. [Online]. Available: https://opg.optica.org/ol/abstract.cfm?uri=ol-40-17-3937

[51] Y.-C. Lu, W.-P. Huang, and S.-S. Jian, "Full vector complex coupled mode theory for tilted fiber gratings," *Opt. Exp.*, vol. 18, no. 2, pp. 713–726, Jan. 2010. [Online]. Available: https://opg.optica.org/oe/abstract.cfm?uri=oe-18-2-713

[52] A. Hale, T. A. Strasser, and P. S. Westbrook, "Optical fiber gratings with index matched polymer coatings for cladding mode suppression," EP Patent EP1 146 357A2, Oct., 2001. [Online]. Available: https://patents.google.com/patent/EP1146357A2/en

[53] J. P. Meunier and S. I. Hosain, "An efficient model for splice loss evaluation in single-mode graded-index fibers," *J. Lightw. Technol.*, vol. 9, no. 11, pp. 1457–1463, Nov. 1991. [Online]. Available: https://ieeexplore.ieee.org/document/97632

[54] P. Sillard et al., "Low-differential-Mode-Group-Delay 9-LP-Mode fiber," *J. Lightw. Technol.*, vol. 34, no. 2, pp. 425–430, Jan. 2016. [Online]. Available: https://ieeexplore.ieee.org/abstract/document/7174947

[55] K. Choutagunta and J. M. Kahn, "Designing high-performance multimode fibers using refractive index optimization," *J. Lightw. Technol.*, vol. 39, no. 1, pp. 233–242, Jan. 2021.

[56] D. Östling and H. E. Engan, "Broadband spatial mode conversion by chirped fiber bending," *Opt. Lett.*, vol. 21, no. 3, pp. 192–194, Feb. 1996. [Online]. Available: https://opg.optica.org/ol/abstract.cfm?uri=ol-21-3-192

[57] S. Ramachandran, "Dispersion-tailored few-mode fibers: A versatile platform for in-fiber photonic devices," *J. Lightw. Technol.*, vol. 23, no. 11, pp. 3426–3443, Nov. 2005. [Online]. Available: https://ieeexplore.ieee.org/document/1561371/

[58] T. Mizunami et al., "Long-period gratings written in few-mode optical fiber by ultraviolet laser exposure," presented at the OSA Advanced Photonics Congress, Washington, DC, USA, Jul. 13–16, 2020, Paper JTu3F.8. [Online]. Available: https://opg.optica.org/abstract.cfm?URI=PSC-2020-JTu3F.8

[59] P. Sillard, D. Molin, M. Bigot-Astruc, H. Maerten, D. V. Ras, and F. Achten, "Low-DMGD 6-LP-Mode fiber," presented at the Opt. Fiber Commun. Conf., San Francisco, CA, USA, Mar. 9–13, 2014, Paper M3F.2. [Online]. Available: https://opg.optica.org/abstract.cfm?uri=OFC-2014-M3F.2

[60] P. Sillard, "Few-mode fibers for space division multiplexing," in *Proc. Opt. Fiber Commun. Conf. Exhib.*, Mar. 2016, pp. 1–53. [Online]. Available: https://ieeexplore.ieee.org/document/7537334

[61] P. Sillard et al., "Few-mode fiber technology, deployments, and systems," *Proc. IEEE*, vol. 110, no. 11, pp. 1804–1820, Nov. 2022. [Online]. Available: https://ieeexplore.ieee.org/document/9906979

[62] Y. Liu, J. Lit, X. Gu, and L. Wei, "Fiber comb filters based on UV-writing Bragg gratings in graded-index multimode fibers," *Opt. Exp.*, vol. 13, no. 21, pp. 8508–8513, Oct. 2005. [Online]. Available: https://opg.optica.org/oe/abstract.cfm?uri=oe-13-21-8508

[63] M. Chomát et al., "Responses of a long-period grating fabricated in a graded-index optical fiber to temperature and refractive-index changes," *Mater. Sci. Eng.: C*, vol. 26, no. 2, pp. 457–461, Mar. 2006. [Online]. Available: https://www.sciencedirect.com/science/article/pii/S0928493105003905

[64] A. Anuszkiewicz et al., "Fused silica optical fibers with graded index nanostructured core," *Sci. Rep.*, vol. 8, no. 1, Aug. 2018, Art. no. 12329. [Online]. Available: https://www.nature.com/articles/s41598-018-30284-1

[65] R. Kasztelanic, H. T. Nguyen, D. Pysz, H. Thienpont, T. Omatsu, and R. Buczynski, "Free-form optical fiber with a square mode and top-hat intensity distribution," *Adv. Sci.*, vol. 11, no. 33, 2024, Art. no. 2402886. [Online]. Available: https://onlinelibrary.wiley.com/doi/abs/10.1002/advs.202402886

[66] R. Buczynski et al., "Optical fibers with gradient index nanostructured core," *Opt. Exp.*, vol. 23, no. 20, Art. no. 25588, Oct. 2015. [Online]. Available: https://opg.optica.org/abstract.cfm?URI=oe-23-20-25588

[67] T. Osuch et al., "Inscription of Bragg gratings in nanostructured graded index single-mode fibers," *Opt. Exp.*, vol. 27, no. 10, pp. 13721–13733, May 2019. [Online]. Available: https://opg.optica.org/oe/abstract.cfm?uri=oe-27-10-13721

[68] T. Osuch et al., "Enhancement of spectral response of Bragg gratings written in nanostructured and multi-stepped optical fibers with radially shaped GeO_2 concentration," *Opt. Exp.*, vol. 28, no. 10, pp. 14774–14787, May 2020. [Online]. Available: https://opg.optica.org/oe/abstract.cfm?uri=oe-28-10-14774

[69] P. Pogorzelski, A. Anuszkiewicz, R. Buczyński, and T. Osuch, "A numerical tool for spectral analysis of fiber Bragg gratings written in few-mode excited optical fibers," *Acta Physica Polonica A*, vol. 146, no. 4, pp. 490–490, Nov. 2024. [Online]. Available: https://appol.ifpan.edu.pl/index.php/appa/article/view/146_490

[70] V. Scarnera, C. A. Codemard, M. Durkin, and M. N. Zervas, "Splice optimisation between dissimilar fibres in the presence of dopant diffusion," *Proc. SPIE*, vol. 12865, Mar. 2024, Art. no. 1286515. [Online]. Available: https://www.spiedigitallibrary.org/conference-proceedings-of-spie/12865/1286515/Splice-optimisation-between-dissimilar-fibres-in-the-presence-of-dopant/10.1117/12.3003118.full

[71] N. K. Fontaine et al., "Broadband 15-mode multiplexers based on multi-plane light conversion with 8 planes in unwrapped phase space," in *Proc. 2022 Eur. Conf. Opt. Commun.*, 2022, pp. 1–4.

[72] S. G. Leon-Saval, N. K. Fontaine, J. R. Salazar-Gil, B. Ercan, R. Ryf, and J. Bland-Hawthorn, "Mode-selective photonic lanterns for space-division multiplexing," *Opt. Exp.*, vol. 22, no. 1, pp. 1036–1044, Jan. 2014. [Online]. Available: https://opg.optica.org/oe/abstract.cfm?URI=oe-22-1-1036

[73] A. M. Velázquez-Benıtéz et al., "Scaling photonic lanterns for space-division multiplexing," *Sci. Rep.*, vol. 8, no. 1, Jun. 2018, Art. no. 8897. [Online]. Available: https://www.nature.com/articles/s41598-018-27072-2

[74] R. I. Becerra-Deana, M. P. de Sivry-Houle, S. Virally, C. Boudoux, and N. Godbout, "Mode-selective photonic lanterns with double-clad fibers," *J. Lightw. Technol.*, vol. 43, no. 12, pp. 5829–5835, Jun. 2025. [Online]. Available: https://opg.optica.org/jlt/abstract.cfm?URI=jlt-43-12-5829

Oleksiy Krutko (Member, IEEE) received the B.S. degree in electrical engineering from the University of Texas at Austin, Austin, TX, USA, in 2020. He is currently working toward the Ph.D. degree with Stanford University, Stanford, CA, USA. His research interests include optical fiber communications and photonic devices.

Rebecca Refaee received the B.S. degree in mathematics and the M.S. degree in electrical engineering from Stanford University, Stanford, CA, USA, in 2024. She is currently working toward the Ph.D. degree in electrical engineering with Stanford University. Her research interests include optical communications and mode-division multiplexing.

Anirudh Vijay (Member, IEEE) received the B.Tech. and M.Tech. degrees in electrical engineering from the Indian Institute of Technology Madras, Chennai, India, in 2019. He is currently working toward the Ph.D. degree in electrical engineering from Stanford University, Stanford, CA, USA. His research interests include optical communications, mode-division multiplexing, and data-center applications.

Nika Zahedi is currently working toward the B.S. and M.S. degrees in electrical engineering with Stanford University, Stanford, CA, USA. Her research interests include mode-division multiplexing, signal processing, and optimization techniques.

Joseph M. Kahn (Life Fellow, IEEE) received the A.B., M.A. and Ph.D. degrees in physics from the University of California, Berkeley, CA, USA, in 1981, 1983 and 1986. From 1987 to 1990, he was with AT&T Bell Laboratories. In 1989, he demonstrated the first successful synchronous (i.e., coherent) detection using semiconductor lasers, achieving record receiver sensitivity. From 1990 to 2003, he was with the Electrical Engineering and Computer Sciences faculty at Berkeley. In 2003, he was a Professor of electrical engineering with E. L. Ginzton Laboratory, Stanford University, Stanford, CA, USA. He demonstrated coherent detection of QPSK, in 1992. In 1999, D. S. Shiu and Kahn authored or coauthored the first work on probabilistic shaping for optical communications. In the 1990s and early 2000s, Kahn and collaborators performed seminal work on indoor and outdoor free-space optical communications and multi-input multi-output wireless communications. In 2000, Kahn and K. P. Ho founded StrataLight Communications, whose 40 Gb/s-per-wavelength long-haul fiber transmission systems were deployed widely by AT&T, Deutsche Telekom, and other carriers. In 2002, Ho and Kahn applied to patent the first electronic compensation of fiber Kerr nonlinearity. StrataLight was acquired by Opnext in 2009. Kahn and collaborators have extensively studied rate-adaptive coding and modulation, and digital signal processing for mitigating linear and nonlinear impairments in coherent systems. In 2008, E. Ip and Kahn (and G. Li independently) invented simplified digital backpropagation for compensating fiber Kerr nonlinearity and dispersion. Since 2004, Kahn and collaborators have been studying propagation, modal statistics, spatial multiplexing and imaging in multi-mode fibers, elucidating principal modes, and demonstrating transmission beyond the traditional bandwidth-distance limit in 2005, deriving the statistics of coupled modal group delays and gains in 2011, and deriving resolution limits for imaging in 2013. His current research interests include optical frequency comb generators, coherent data center links, rate-adaptive access networks, fiber Kerr nonlinearity mitigation, ultra-long-haul submarine links, and optimal free-space transmission through atmospheric turbulence. He was the recipient of the National Science Foundation Presidential Young Investigator Award in 1991.